Draft version October 10, 2020
Typeset using LaTeX **twocolumn** style in AASTeX63

Source Counts Spanning Eight Decades of Flux Density at 1.4 GHz

A. M. Matthews [1,2] J. J. Condon [2] W. D. Cotton [2] and T. Mauch [3]

[1] *Department of Astronomy, University of Virginia, Charlottesville, VA 22904, USA*
[2] *National Radio Astronomy Observatory, 520 Edgemont Road, Charlottesville, VA 22903, USA*
[3] *South African Radio Astronomy Observatory (SARAO), 2 Fir Street, Black River Park, Observatory, 7925, South Africa*

ABSTRACT

Brightness-weighted differential source counts $S^2n(S)$ spanning the eight decades of flux density between 0.25 μJy and 25 Jy at 1.4 GHz were measured from the confusion brightness distribution in the MeerKAT DEEP2 image below 10 μJy, counts of individual DEEP2 sources between 10 μJy and 2.5 mJy, and counts of NVSS sources stronger than 2.5 mJy. The brightness-weighted counts converge as $S^2n(S) \propto S^{1/2}$ below $S = 10\,\mu$Jy, so $> 99\%$ of the $\Delta T_\mathrm{b} \sim 0.06$ K sky brightness produced by active galactic nuclei and $\approx 96\%$ of the $\Delta T_\mathrm{b} \sim 0.04$ K added by star-forming galaxies has been resolved into discrete sources with $S \geq 0.25\,\mu$Jy. The $\Delta T_\mathrm{b} \approx 0.4$ K excess brightness measured by ARCADE 2 cannot be produced by faint sources smaller than ≈ 50 kpc if they cluster like galaxies.

Keywords: galaxies: evolution – galaxies: star formation – galaxies: statistics – radio continuum: galaxies

1. INTRODUCTION

The differential source count $n(S)dS$ at frequency ν is the number of sources per steradian with flux densities between S and $S + dS$. The Rayleigh-Jeans sky brightness temperature dT_b per decade of flux density added by these sources is

$$\left[\frac{dT_\mathrm{b}}{d\log(S)}\right] = \left[\frac{\ln(10)\,c^2}{2k_\mathrm{B}\nu^2}\right] S^2 n(S)\ , \qquad (1)$$

where $k_\mathrm{B} \approx 1.38 \times 10^{-23}\,\mathrm{J\,K^{-1}}$. This paper presents 1.4 GHz brightness-weighted source counts $S^2n(S)$ covering the eight decades of flux density between $S = 0.25\,\mu$Jy and $S = 25$ Jy based on the very sensitive $\nu = 1.266$ GHz MeerKAT DEEP2 sky image (Mauch et al. 2020) confusion brightness distribution between $S = 0.25\,\mu$Jy and $S = 10\,\mu$Jy, the DEEP2 discrete source catalog from $S = 10\,\mu$Jy to $S = 2.5$ mJy, and on the 1.4 GHz NRAO VLA Sky Survey (Condon et al. 1998, NVSS) catalog above $S = 2.5$ mJy. Nearly all of these sources are extragalactic.

The 1.266 GHz DEEP2 image covers the $\Theta_{1/2} = 69\farcm2$ diameter half-power circle of the MeerKAT primary beam centered on J2000 $\alpha = 04^\mathrm{h}\,13^\mathrm{m}\,26\fs4$, $\delta = -80°\,00'\,00''$. Its point-source response is a $\theta_{1/2} = 7\farcs6$ FWHM Gaussian, and the rms noise is $\sigma_\mathrm{n} = 0.56 \pm 0.01\,\mu\mathrm{Jy\,beam^{-1}}$ at the pointing center. The DEEP2 image is strongly confusion limited, so we could not treat its position and flux-density error distributions analytically. Therefore we created radio sky simulations (Section 2) to model the statistical source counts consistent with the confusion brightness distribution, refine our catalog of discrete DEEP2 sources, and correct our counts of the faintest sources.

Statistical source counts between $S = 0.25\,\mu$Jy and $S = 10\,\mu$Jy (Section 3) were estimated from the confusion $P(D)$ distribution within $500''$ of the DEEP2 pointing center. We constructed a uniformly sensitive catalog of $\approx 17,000$ discrete sources stronger than $S = 10\,\mu$Jy at 1.266 GHz inside the primary half-power circle (Section 4) and used it to count discrete sources in the flux-density range $10\,\mu\mathrm{Jy} \leq S < 2.5$ mJy (Section 5). The NVSS catalog of radio source components was used to determine 1.4 GHz source counts between $S = 2.5$ mJy and $S = 25$ Jy in the $\Omega \approx 7.016$ sr defined by $\delta \geq -40°$ and $|b| \leq 20°$ (Section 6). Section 7 summarizes the 1.4 GHz counts of sources as faint as $S = 0.25\,\mu$Jy and discusses their significance in terms of known populations of extragalactic sources powered by active galactic nuclei (AGNs) or by star formation in star-forming galaxies (SFGs) plus possible "new" populations of radio sources.

Corresponding author: Allison M. Matthews
amm4ws@virginia.edu

Absolute quantities in this paper were calculated for a ΛCDM universe with $H_0 = 70\,\mathrm{km\,s^{-1}\,Mpc^{-1}}$ and $\Omega_\mathrm{m} = 0.3$ using equations in Condon & Matthews (2018). Our spectral-index sign convention is $\alpha \equiv +d\ln S/d\ln\nu$.

2. THE RADIO SKY SIMULATIONS

The confusion brightness distribution can be calculated analytically only for scale free power-law differential source counts of the form $n(S) \propto S^{-\gamma}$ (Condon 1974). Likewise, biases in counts of faint discrete sources can easily be estimated only in the power-law count approximation (Murdoch et al. 1973). The actual source counts near $S \sim 10\,\mu$Jy are not well approximated by a single power law, so we used computer simulations of the 1.266 GHz DEEP2 image to estimate statistical source counts below 10 μJy from the DEEP2 image brightness distribution and to correct for biases in the DEEP2 discrete source counts above 10 μJy. We simulated only point sources because the measured median angular diameter $\langle\phi\rangle \approx 0\farcs3$ of real μJy sources (Cotton et al. 2018) is much smaller than the DEEP2 restoring beam diameter $\theta_{1/2} = 7\farcs6$ (Mauch et al. 2020) and only ∼ 0.2% of the DEEP2 sources stronger than $S = 10\,\mu$Jy are clearly resolved (Section 4.4). The simulated sources all have spectral index $\alpha = -0.7$, the median spectral index of extragalactic sources (Condon 1984).

The input for each simulation is an arbitary user-specified 1.266 GHz source count $n(S)$. In every flux-density bin of width $\Delta\log(S) = 0.001$ the actual number of simulated sources is chosen by a random-number generator sampling the Poisson distribution whose mean matches the input $n(S)$. The sources are scattered randomly at the centers of $1\farcs25 \times 1\farcs25$ pixels covering a square larger than the $\Theta_{1/2} = 69\farcm2$ DEEP2 half-power circle. The real μJy sources in DEEP2 are nearly all extragalactic and very distant (median redshift $\langle z\rangle \sim 1$), so they are spread out over a radial distance range $\Delta z \sim 1$ much larger than the galaxy correlation length and their sky distribution is quite random and isotropic (Benn & Wall 1995; Condon & Matthews 2018), unlike the visibly clustered sky distribution of nearby optically selected galaxies. In addition, clustering appears to have little effect on FIR, millimeter, and radio confusion brightness distributions observed with the resolutions close to the $\theta_{1/2} = 7\farcs6$ DEEP2 restoring beam diameter (Béthermin et al. 2017).

The simulations also reproduce the DEEP2 observational effects and imaging processes described by Mauch et al. (2020). The 1.266 GHz wideband DEEP2 image is the average of 14 narrow subband images weighted to maximize the signal-to-noise ratio (SNR) of sources with spectral index $\alpha = -0.7$ (Table 1). The dirty DEEP2 image was CLEANed down to residual peak flux density $S_\mathrm{p} = 5\,\mu\mathrm{Jy\,beam^{-1}}$. The simulated image replicates CLEANing by representing each source as the sum of two components: (1) a component whose brightness distribution is the DEEP2 dirty beam and whose peak flux density is the lesser of the input source flux density or 5 μJy plus (2) a CLEAN component whose brightness distribution is the circular Gaussian restoring beam of FWHM $\theta_{1/2} = 7\farcs6$ and whose amplitude is the difference between the input source flux density and 5 μJy. The dirty beam used for each subband of the simulation is the same the actual DEEP2 subband dirty beam.

Table 1. DEEP2 imaging subband frequencies and weights

Subband number	ν_i (MHz)	σ_i (μJy beam^{-1})	w_i for min σ_n^2	w_i for max SNR
$i = 1$	908.040	4.224	0.0225	0.0378
2	952.340	5.044	0.0158	0.0248
3	996.650	3.196	0.0393	0.0580
4	1043.460	2.882	0.0483	0.0669
5	1092.780	2.761	0.0526	0.0683
6	1144.610	2.580	0.0603	0.0733
7	1198.940	4.203	0.0227	0.0259
8	1255.790	3.981	0.0253	0.0271
9	1317.230	1.851	0.1171	0.1170
10	1381.180	1.643	0.1486	0.1389
11	1448.050	1.549	0.1672	0.1463
12	1519.940	1.871	0.1147	0.0938
13	1593.920	2.888	0.0481	0.0368
14	1656.200	1.850	0.1173	0.0850

NOTE—Column 1 is the subband number i, column 2 the subband central frequency ν_i, column 3 the rms noise σ_i in the subband image, and column 5 is the subband image weight w_i used to produce the wideband DEEP2 image with the highest signal-to-noise ratio (SNR) for sources with spectral index $\alpha = -0.7$.

The simulation generates sources with spectral index $\alpha = -0.7$ and combines the subband images with the weights listed in column 5 of Table 1. To simulate the DEEP2 primary beam attenuation, the subband images were multiplied by the frequency-dependent MeerKAT primary beam specified by equations 3 and 4 in Mauch et al. (2020). After multiplying by the primary beam attenuation, the simulation adds to each pixel of the wideband image a randomly generated sample of Gaussian noise. The noise in an aperture-synthesis image has the same (u, v)-plane coverage as the signal, so the DEEP2 image noise is smoothed by the same dirty beam. To replicate this, the simulation convolved the pixel noise distribution with the dirty beam. The rms amplitude of the convolved noise usually was set to match observed

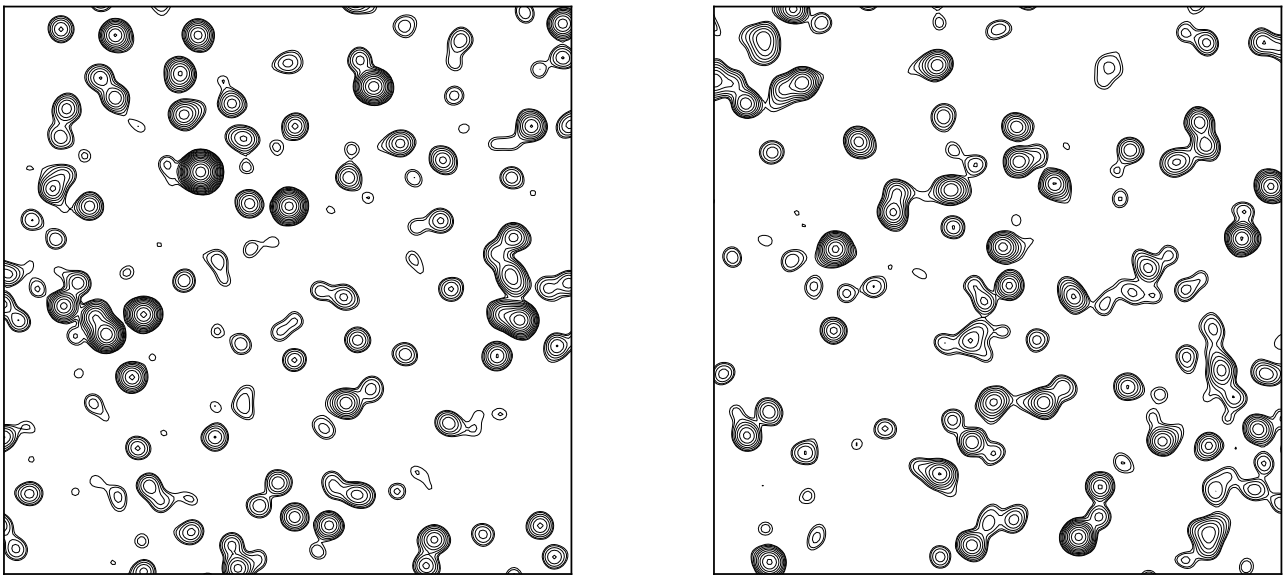

Figure 1. These contour plots compare $4.2' \times 4.2'$ regions of one DEEP2 simulation (left panel) and the actual DEEP2 image (right panel). Contours are drawn at 1.266 GHz peak flux densities $S_p = \pm 5\,\mu\text{Jy beam}^{-1} \times (2^0, 2^{0.5}, 2^1, 2^{1.5}, ...)$.

rms noise $\sigma_n = 0.56 \pm 0.01\,\mu\text{Jy beam}^{-1}$ in the actual DEEP2 image prior to correction for primary beam attenuation.

Finally, this simulated image must be divided by primary beam attenuation to yield a simulated sky image. Figure 1 compares $4\farcs2 \times 4\farcs2$ (200×200 pixels) cutouts from one simulated sky image with the actual DEEP2 sky image to show that the simulated image looks like the real image.

3. THE DEEP2 $P(D)$ DISTRIBUTION

The term "confusion" refers to fluctuations in sky brightness caused by multiple faint sources inside the point-source response. Historically confusion described by the probability distribution $P(D)$ of pen deflections of magnitude D on a chart-recorder plot of detected power (Scheuer 1957). The analog of the deflection D at any pixel in a modern radio image is the sky brightness expressed as a peak flux density (flux density per beam solid angle) S_p, so the $P(D)$ distribution could appropriately be renamed the $P(S_p)$ distribution.

The peak flux density S_p at any point in an image is the sum of contributions from noise-free source confusion and image noise. Confusion and noise are independent, so the observed $P(D)$ distribution is the convolution of the confusion and noise distributions. The noise amplitude distribution in an aperture-synthesis image is much easier to deconvolve because it is extremely stable, Gaussian, and uniform across the image prior to correction for primary-beam attenuation (Condon et al. 2012), unlike the noise in a single-dish image, which varies significantly with position and time during an observation. Consequently we were able to measure the DEEP2 rms noise $\sigma_n = 0.56 \pm 0.01\,\mu\text{Jy beam}^{-1}$ (not corrected for primary attenuation) and confirm its Gaussian amplitude distribution with very small uncertainties. The noise distribution is narrower than the noiseless $P(D)$ distribution in the very sensitive DEEP2 image, so we could deconvolve the Gaussian noise distribution from the observed $P(D)$ distribution to calculate the desired noiseless $P(D)$ distribution with unprecedented accuracy and sensitivity.

We extracted the $P(D)$ distribution from the circle of radius $r = 500''$ covering solid angle $\Omega = 1.85 \times 10^{-5}$ sr centered on the SNR-weighted 1.266 GHz DEEP2 image corrected for primary-beam attenuation and presented as figure 11 in Mauch et al. (2020). The $P(D)$ circle is small enough ($r \ll \Theta_{1/2}/2$) that the mean primary-beam attenuation is 0.98 inside the circle and 0.96 at the edge, so its rms noise after correction for primary-beam attenuation is only $\sigma_n = (0.56 \pm 0.01\,\mu\text{Jy beam}^{-1})/0.98 = 0.57 \pm 0.01\,\mu\text{Jy beam}^{-1}$. The $P(D)$ circle is still large enough to cover $N_b = 1.20 \times 10^4$ restoring beam solid angles $\Omega_b = \pi\theta_{1/2}^2/(4 \ln 2) = 1.54 \times 10^{-9}$ sr. The solid angle of the *square* of the restoring beam attenuation pattern determines the number of independent samples per unit solid angle of sky (Condon et al. 2012). For a Gaussian restoring beam, the solid

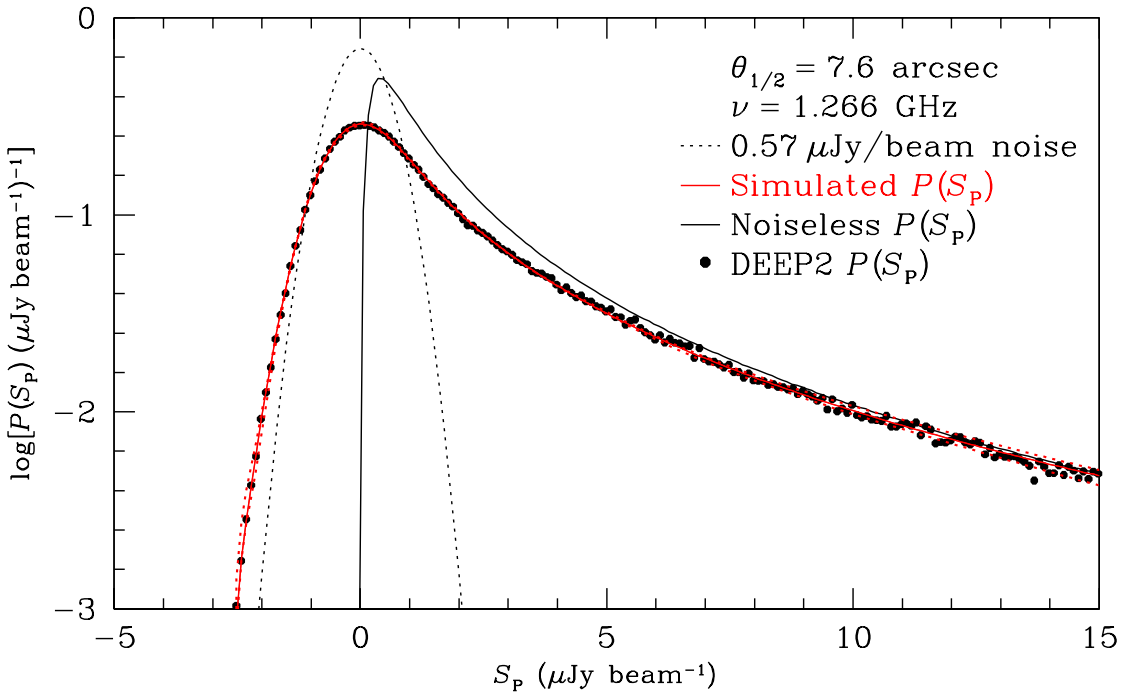

Figure 2. The normalized 1.266 GHz $P(S_p) = P(D)$ distribution extracted from the central $r = 500''$ circle in the $\theta_{1/2} = 7.''6$ resolution DEEP2 image corrected for primary beam attenuation is shown by the heavy black dots representing bins of width $\Delta S_p = 0.1\,\mu$Jy beam^{-1}. It is quite smooth because it is based on 2.40×10^4 independent samples. The dotted parabola on this semilogarithmic plot represents the $\sigma_n = 0.57\,\mu$Jy beam^{-1} Gaussian noise distribution. The red curve is the mean of 1000 simulated $P(D)$ distributions based on the best-fit source counts specified by Equation 3, and the red dotted curves bound the range that includes 2/3 of those simulated $P(D)$ distributions. The black curve shows the best-fit noiseless $P(D)$ distribution.

angle of the beam squared is half the beam solid angle, so the observed DEEP2 $P(D)$ distribution shown in Figure 2 actually contains $2N_b = 2.40 \times 10^4$ statistically independent samples. The observed $P(D)$ distribution (large black points in Figure 2) is the convolution of the noiseless sky $P(D)$ distribution (black curve) with the $\sigma_n = 0.57 \pm 0.01\,\mu$Jy beam^{-1} Gaussian noise distribution accurately represented by the parabolic dotted curve in the semi-logarithmic Figure 2.

The 1.266 GHz DEEP2 $P(D)$ distribution shown in Figure 2 is 4× as sensitive to point sources with $\alpha \approx -0.7$ as the most sensitive published 3 GHz $P(D)$ distribution (Condon et al. 2012). Such sources are 1.83× stronger at 1.266 GHz than at 3 GHz, so the rms noise $\sigma_n = 1.255\,\mu$Jy beam^{-1} of the 3 GHz $P(D)$ distribution is equivalent to $\sigma_n = 2.30\,\mu$Jy beam^{-1} at 1.266 GHz. The peak of the DEEP2 noise distribution is higher than the peak of the noiseless $P(D)$ distribution (Figure 2), indicating that DEEP2 is strongly confusion limited, while the peak of the 3 GHz noise distribution is only half as high as the peak of the peak of the 3 GHz noiseless $P(D)$ distribution. The DEEP2 $P(D)$ distribution also has smaller statistical uncertainties because it includes 3.1× as many independent samples. Finally, the 1.266 GHz DEEP2 $P(D)$ distribution was extracted from the very center of the image where the primary beam attenuation ≥ 0.96, so systematic errors caused by antenna pointing fluctuations or primary beam corrections are negligible.

3.1. $P(D)$ *statistical counts of nJy sources*

The noiseless confusion $P(D)$ distribution is sensitive to the differential counts $n(S)$ of sources more than 10× fainter than the usual $5\sigma_n$ detection limit for individual sources. In terms of the number $N(> S)$ of sources per steradian stronger than S, the mean number of sources stronger than S per beam solid angle Ω_b is $\mu = [N(> S)\Omega_b]$ and the Poisson probability that *all* sources in a beam are weaker than S is $P_P = \exp(-\mu)$. For the DEEP2 image $\Omega_b \approx 1.54 \times 10^{-9}$ sr and the best fit source counts from Equation 3, $P_P \approx 0.4$ at $S = 0.25\,\mu$Jy beam^{-1}. The DEEP2 $P(D)$ distribution was extracted from a solid angle containing 2.40×10^4 independent samples of the sky, so changes in the source count below $S = 0.25\,\mu$Jy beam^{-1} could be detected statistically from the 10^4 independent samples that contain only fainter sources if the noise is low enough.

The DEEP2 $P(D)$ distribution is smoothed by Gaussian noise with rms $\sigma_n = 0.57 \pm 0.01\,\mu$Jy beam^{-1} which degrades its sensitivity to significantly fainter sources.

To estimate the sensitivity of DEEP2 to faint sources in the presence of noise, we simulated noisy $P(D)$ distributions using a variety of differential source counts below $S = 10\,\mu$Jy. Above $S = 10\,\mu$Jy, we used the direct source counts from DEEP2 and the NVSS presented in Sections 5 and 6. The simulation accepts brightness-weighted differential source counts $S^2n(S)$ specified in bins of width $\Delta\log(S) = 0.2$. Directly binning counts $n(S)$ that vary rapidly with S can introduce a significant bias (Jauncey 1968). We mitigated this bias by binning the quantity $S^2n(S)$ which changes little across a flux-density bin.

We ran simulations assuming the following functional forms for $S^2n(S)$ in the flux range $-8 < \log[S(\mathrm{Jy})] < -4.9$: cubic polynomials, the cumulative distribution function of the lognormal probability density function, and curved power laws $n(S) \propto S^{a+bS}$. To measure goodness-of-fit for each input source count we defined a statistic that quadratically combines the reduced χ^2 from differences between the simulated and observed $P(D)$ distributions for all $S_p < 15\,\mu\mathrm{Jy\,beam^{-1}}$ with the χ^2 of the differences between the simulated counts and the direct counts of DEEP2 sources in bins centered on $\log S = -4.9$ and -4.7:

$$\chi^2 = \sqrt{\left(\chi^2_{P(D)}\right)^2 + \left(\chi^2_{\mathrm{DC}}\right)^2}. \qquad (2)$$

Before calculating the value of this statistic for a given simulation, we removed the brightness zero-point offset between the simulated and observed $P(D)$ distributions. Numerous faint radio sources produce a smooth background which is invisible to MeerKAT and other correlation interferometers lacking zero-spacing data. Thus the brightness zero level of our observed $P(D)$ distribution is unknown and must be fitted out. We minimized the zero-level offset by comparing the observed and simulated $P(D)$ distributions shifted in steps of $0.001\,\mu\mathrm{Jy\,beam^{-1}}$, the step size being smaller than the rms noise divided by the square root of the number 2.40×10^4 of independent samples in the DEEP2 $P(D)$ area.

We optimized the parameters for these functional forms by minimizing Equation 2. We inspected the residuals $\Delta N/\sigma_N$, where N is the number of independent samples per bin and σ_N is the Poisson error per bin associated with the observed $P(D)$ distribution, of the resulting best-fits for the presence of correlations as a function of brightness D. The existence of a signal akin to red-noise in our residuals would imply our counts under- or over-estimate the counts of sources in specific flux density ranges.

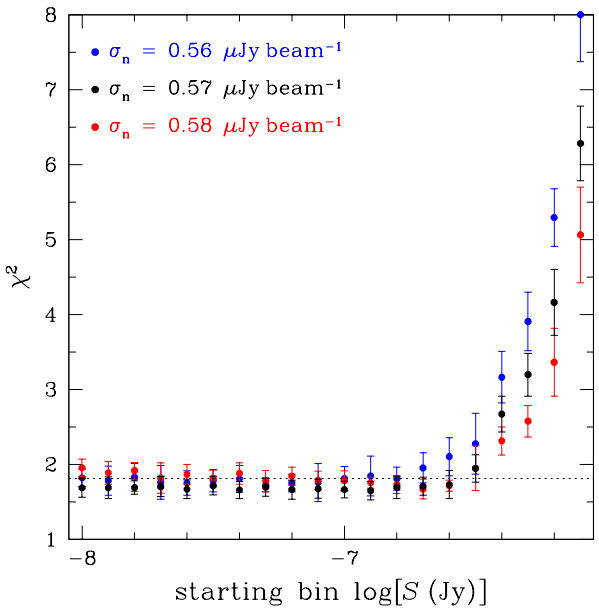

Figure 3. The reduced χ^2 statistic from 1.266 GHz DEEP2 simulations is shown as a function of the starting source count bin increasing from the nominal $\log[S(\mathrm{Jy})] = -8$ to -6.1. At $\log[S(\mathrm{Jy})] = -6.5$, the χ^2 statistic of the $P(D)$ distribution from DEEP2 simulations with $\sigma_\mathrm{n} = 0.57\,\mu$Jy averaged over the $r = 500''$ $P(D)$ circle (black points) exceeds the value of the mean minimum χ^2 plus 1σ (black dotted line). This indicates that we are sensitive to changes in the source count down to $\log[S(\mathrm{Jy})] = -6.6$. The χ^2 values for DEEP2 simulations with $\pm1\sigma$ in rms noise are shown in blue and red for 0.56 and $0.58\,\mu\mathrm{Jy\,beam^{-1}}$, respectively.

The 3rd-degree polynomial source count

$$\begin{aligned}\log[S^2n(S)] = 2.718 &+ 0.405(\log S + 5) \\ &- 0.020(\log S + 5)^2 \\ &+ 0.019(\log S + 5)^3\ ,\end{aligned} \qquad (3)$$

where S is the 1.266 GHz flux density in Jy, gave the simulated $P(D)$ distribution (red curve in Figure 2) best fitting the observed distribution (black points) while maintaining continuity in the transition from the $P(D)$ to direct counts at $S = 10\,\mu$Jy. Although the simulation includes sources as faint as $S = 0.01\,\mu$Jy, the DEEP2 image is not sensitive to the counts of such faint sources. The biggest cause of uncertainty in our sub-μJy source counts is the $\pm0.01\,\mu\mathrm{Jy\,beam^{-1}}$ uncertainty in the DEEP2 rms noise. To estimate the flux density of the faintest sources we can usefully count, we set the rms noise to $\sigma_\mathrm{n} = 0.57\,\mu\mathrm{Jy\,beam^{-1}}$ and iteratively removed the lowest flux-density bin before using that sub-sample of bins to produce the DEEP2 simulation. After repeating this process for a total of 50 trials, we found that removing the source count bin at $\log[S(\mathrm{Jy})] = -6.6$ in-

creases the simulation χ^2 to more than one-sigma above the mean minimum χ^2, as shown by the the black points above the dotted line in Figure 3. The same process was repeated for for $\sigma_{\rm n} = 0.56\,\mu{\rm Jy\,beam^{-1}}$ (blue points) and $0.58\,\mu{\rm Jy\,beam^{-1}}$ (red points). The results are consistent with a count sensitivity limit $\log[S({\rm Jy})] \approx -6.6$ or $S \approx 0.25\,\mu{\rm Jy}$.

To determine the sensitivity of our best-fitting $P(D)$ distribution above $S = 0.25\,\mu{\rm Jy}$ to small changes in the rms noise, we ran 1000 simulations of the DEEP2 $P(D)$ distribution using the counts given by Equation 3 and varying the $\sigma_{\rm n} = 0.57\,\mu{\rm Jy\,beam^{-1}}$ noise by adding values drawn randomly from a Gaussian distribution of rms width $0.01\,\mu{\rm Jy\,beam^{-1}}$. The range of $P(D)$ containing 68% of these simulations best fitting (according to Equation 2) the average of all 1000 simulations defines the 1σ uncertainty region of our model $P(D)$. Figure 2 includes dotted red lines showing this narrow uncertainty region, which is easily visible only in the $S_{\rm p} > 10\,\mu{\rm Jy\,beam^{-1}}$ tail of the distribution.

To estimate the 1σ source-count errors resulting from the above $P(D)$ distribution range, we ran 500 simulations with the following variations: (1) the noise was drawn randomly from Gaussion distributions with mean rms $\sigma_{\rm n} = 0.57\,\mu{\rm Jy\,beam^{-1}}$ and scatter $0.01\,mu{\rm Jy\,beam^{-1}}$; (2) the input source counts were modeled with a fourth-degree polynomial to allow for the rapidly growing count uncertainty at the lowest flux densities caused by noise as well as by a possible "new" population of very faint radio sources; and (3) the coefficients of the fourth-degree polynomials were drawn randomly from gaussian distributions centered on the best-fitting values given in Equation 3 with an rms of 0.1 (the unknown fourth-degree coefficient was intially centered on zero).

Each combination of coefficients and rms noise was repeated an additional six times to determine the effects of noise on the goodness-of-fit. We considered a set of coefficients to be in agreement with the DEEP2 $P(D)$ distribution if at least five of the total seven simulations fell within the 1σ uncertainty region determined from the original, un-altered 1000 simulations. The subset of the 500 coefficent-varying simulations that satisfied this criterion define the statistical uncertainty of the measured source counts. Then we added quadratically a 3% count uncertainty to absorb possible 3% systematic flux-density calibration errors. In the flux density range $-6.6 < \log[S({\rm Jy})] < 5$, the 1-$\sigma$ lower limit of the 1.266 GHz source-count error region is

$$\begin{aligned}\log[S^2 n(S)] = 2.677 &+ 0.489(\log S + 5) \\ &+ 0.077(\log S + 5)^2 \\ &+ 0.061(\log S + 5)^3 \\ &- 0.058(\log S + 5)^4\end{aligned} \tag{4}$$

and the 1-σ upper limit is

$$\begin{aligned}\log[S^2 n(S)] = 2.768 &+ 0.367(\log S + 5) \\ &- 0.076(\log S + 5)^2 \\ &- 0.009(\log S + 5)^3 \\ &+ 0.023(\log S + 5)^4\ .\end{aligned} \tag{5}$$

We converted the 1.266 GHz flux densities and brightness-weighted source counts in Equations 3, 4, and 5 to the common source-count frequency $\nu = 1.4$ GHz for sources with spectral index $\alpha = -0.7$ using

$$\begin{aligned}\log(S_{1.4\,{\rm GHz}}) &= \log(S_{1.266\,{\rm GHz}}) + \alpha \log\left(\frac{1.4}{1.266}\right) \\ &\approx \log(S_{1.266\,{\rm GHz}}) - 0.0306\end{aligned} \tag{6}$$

and

$$\begin{aligned}\log[S^2 n(S)]_{1.4\,{\rm GHz}} &= \log[S^2 n(S)]_{1.266\,{\rm GHz}} + \alpha \log\left(\frac{1.4}{1.266}\right) \\ &\approx \log[S^2 n(S)]_{1.266\,{\rm GHz}} - 0.0306\ .\end{aligned} \tag{7}$$

We also calculated the commonly used static-Euclidean source counts from the brightness-weighted source counts via

$$\log[S^{5/2} n(S)] = 0.5 \log(S) + \log[S^2 n(S)]\ . \tag{8}$$

Our 1.4 GHz differential source counts with both normalizations are plotted in Figure 4.

4. THE DEEP2 DISCRETE SOURCE CATALOG

The "effective frequency" of the wideband SNR-weighted DEEP2 image for sources with median spectral index $\langle\alpha\rangle \approx -0.7$ is $\nu_{\rm e} = 1.266$ GHz (Mauch et al. 2020). Even after correction for primary-beam attenuation, the DEEP2 image is strongly confusion limited with rms noise $\sigma_{\rm n} < 1.12\,\mu{\rm Jy\,beam^{-1}}$ everywhere inside the primary beam half-power circle, so we used the attenuation-corrected "sky" image to search for discrete sources. Consequently our catalog brightness sensitivity limit $S_{\rm p}(1.266\,{\rm GHz}) = 10\,\mu{\rm Jy\,beam^{-1}} > 9\sigma_{\rm n}$ is uniform over the whole primary half-power circle of diameter $\Theta_{1/2} = 69\farcm2$ covering solid angle $\Omega = 3.182 \times 10^{-4}$ sr, unlike the variable sensitivity limit of a deep source catalog extracted from an image still attenuated by the

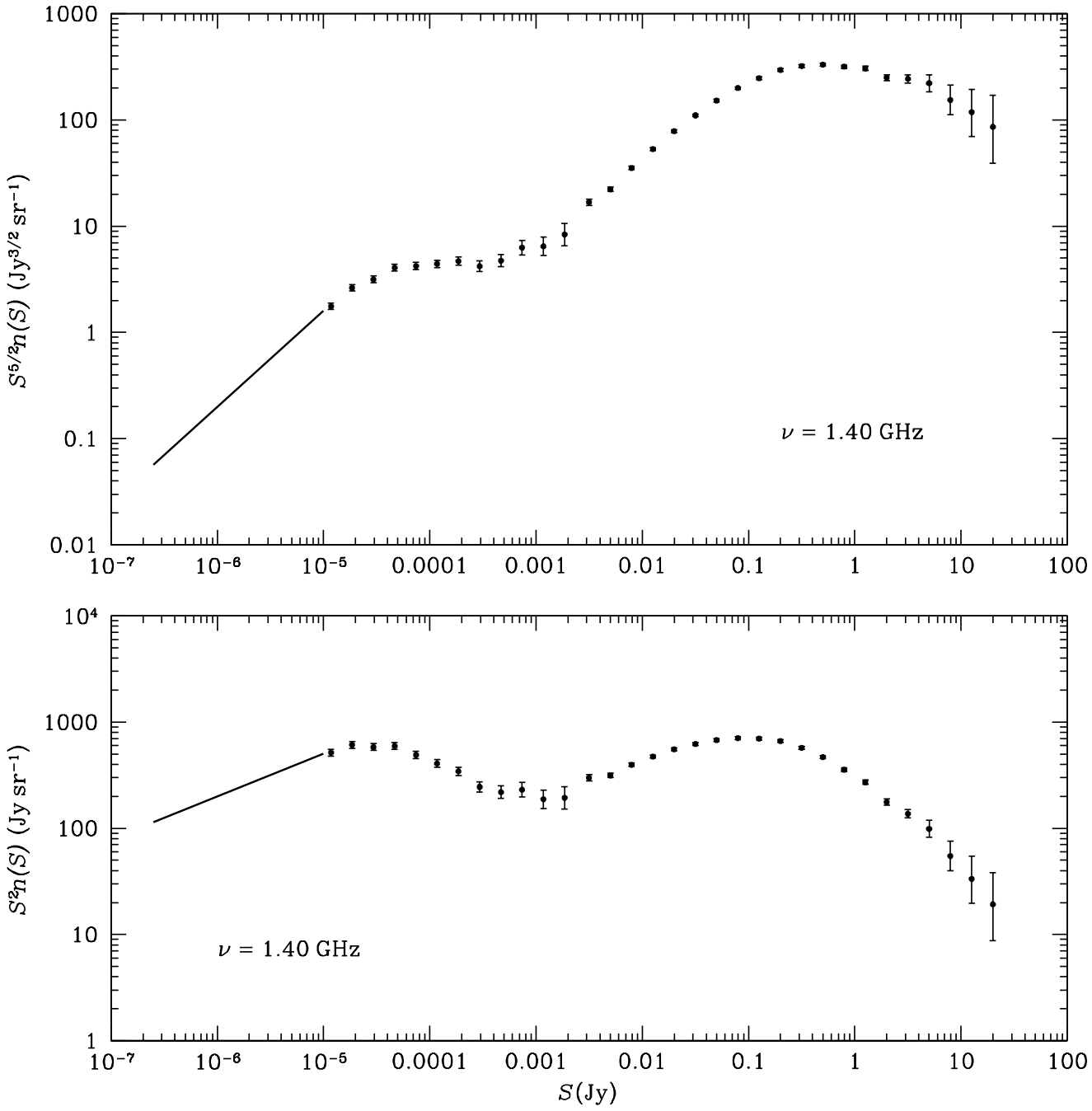

Figure 4. Our 1.4 GHz differential source counts between 0.25 μJy and 25 Jy are shown with both the traditional static Euclidean normalization $S^{5/2}n(S)$ (top panel) and the brightness-weighted normalization $S^2n(S)$ (bottom panel). The heavy curve and light $\pm1\,\sigma$ error curves from $S = 2.5 \times 10^{-7}$ Jy to 10^{-6} Jy are statistical counts derived from the DEEP2 confusion $P(D)$ distribution (Section 3). The black data points and their $\pm1\,\sigma$ error bars show the 1.4 GHz DEEP2 source counts between $S = 10^{-5}$ Jy and $S = 0.0025$ Jy (Section 4) plus the NVSS counts (Section 6) at higher flux densities.

primary beam. Nearly all μJy radio sources are unresolved by the $\theta_{1/2} = 7\farcs6$ DEEP2 restoring beam, so the DEEP2 source catalog should be nearly complete for sources with total flux densities just above $S(1.266\,\mathrm{GHz}) = 10\,\mu\mathrm{Jy}$. The relatively large DEEP2 restoring beam is actually advantageous because incompleteness corrections for partially resolved sources can be large and uncertain when the beam size is not much larger than the median source size (Morrison et al. 2010; Owen 2018).

4.1. *The DEEP2 Component Catalog*

We applied the *Obit* (Cotton 2008) source-finding task FndSou to the DEEP2 sky image inside the DEEP2 primary beam half-power circle centered on J2000 $\alpha = 04^\mathrm{h}\,13^\mathrm{m}\,26\farcs4$, $\delta = -80^\circ\,00'\,00''$. FndSou searches for islands of contiguous pixels and decomposes each island into elliptical Gaussians components as faint as $S_\mathrm{p} = 10\,\mu\mathrm{Jy\,beam}^{-1}$. Most radio sources with $S(3\,\mathrm{GHz}) \gtrsim 5\,\mu$Jy (equivalent to $S \gtrsim 9\,\mu$Jy at 1.266 GHz for $\langle\alpha\rangle = -0.7$) have angular diameters $\phi \lesssim 0\farcs66$ (Cotton et al. 2018) and would be completely unresolved by the $\theta_{1/2} = 7\farcs6$ DEEP2 restoring beam. This point-source approximation is supported by the qualitative similarity of our point-source simulation and the actual DEEP2 image shown in Figure 1. A small fraction of the radio sources stronger than $\sim 100\,\mu$Jy are clearly resolved, and they can be represented by combining multiple components as described in Section 4.4.

The sky density of sources reaches one per 25 restoring beam solid angles at $S(1.266\,\mathrm{GHz}) \approx 17\,\mu$Jy (Mauch et al. 2020), so a significant fraction of our $S \gtrsim 10\,\mu$Jy components partially overlap, and our catalog accuracy, completeness, and reliability are limited more by confusion than by noise. To optimize the DEEP2 component catalog and understand its limitations, we used FndSou to extract catalogs of components from simulated images and compared those catalogs with the simulation input source lists. We compared catalogs in which the fitted elliptical Gaussians were allowed to vary in width to "point source" catalogs in which they were fixed at $\theta_{1/2} = 7\farcs6$ and found that forcing point-source fits generally gave better matches to the "true" simulation input catalogs. Therefore we forced point-source fits to make the DEEP2 component catalog, and we later combined components as needed to represent multicomponent extended radio sources.

In a few crowded regions, FndSou reported spurious faint components very close to much stronger sources. To decide which components to reject from our catalog, we generalized the original Rayleigh criterion for resolving two equal point sources observed with an Airy pattern PSF: the peak of one lies on or outside the first zero of the second, which ensures that the total response has a minimum between them.

The total image response R at position x between unequal components S_1 at $x_1 = 0$ and $S_2 < S_1$ at $x_2 = \Delta$ to a Gaussian PSF with FWHM $\theta_{1/2}$ is

$$R = S_1 \exp\left(-\frac{4\ln 2}{\theta_{1/2}^2}x^2\right) + S_2 \exp\left[-\frac{4\ln 2}{\theta_{1/2}^2}(x-\Delta)^2\right]. \quad (9)$$

For R to have a minimum between the components, $dR/dx = 0$ for some $0 < x < \Delta$. The continuous curve in Figure 5 shows the required component separation $\Delta/\theta_{1/2}$ as a function of the flux-density ratio S_1/S_2. All DEEP2 catalog components stronger than

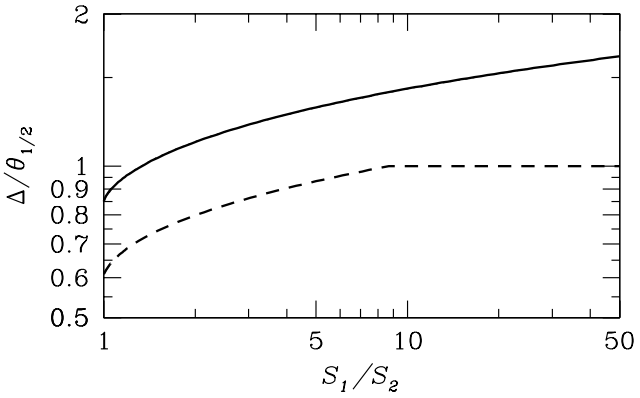

Figure 5. The continuous curve shows the calculated minimum separation Δ in Gaussian beamwidths $\theta_{1/2}$ needed to produce a minimum between two point sources as a function of their flux-density ratio S_1/S_2. The dashed curve shows the empirical minimum separation for reliable DEEP2 components stronger than $10\,\mu$Jy.

$S > 10\,\mu$Jy have SNR> 9, so the requirement in Equation 9 is stricter than necessary. By comparing ten catalogs of components extracted from simulated images with the "true" input components used to generate the simulated images, we found that faint components near stronger components are reliable if they satisfy the weaker criterion

$$\begin{aligned} \frac{\Delta}{\theta_{1/2}} &\geq 0.574 + 0.357[\log(S_1/S_2) + 0.01]^{1/2} + \\ &\quad 0.082\log(S_1/S_2) && \text{if } (S_1/S_2) < 9 \\ \frac{\Delta}{\theta_{1/2}} &\geq 1 && \text{if } (S_1/S_2) \geq 9 \end{aligned} \quad (10)$$

shown by the dashed curve in Figure 5. We rejected the 334 probably spurious DEEP2 components ($< 2\%$ of the total) failing to satisfy Equation 10.

To estimate the effects of confusion and noise on the completeness, reliability, positions, and flux densities of the surviving 17,350 DEEP2 components, we ran ten independent simulations of the DEEP2 field out to the half-power circle of the primary beam using input source counts consistent with the differential source counts in Table 4 and the 1.4 GHz statistical count $S^2 n(S) = 1.07 \times 10^{-5} S^{-0.48}\,\mathrm{Jy\,sr^{-1}}$ of fainter sources from Mauch et al. (2020). For each simulated image, we used FndSou to find all components stronger than $10\,\mu$Jy and rejected the components that did not satisfy the resolution criterion in Equation 10. The positions and flux densities of the resulting ten catalogs were compared with the "true" simulation input positions and flux densities of all simulated sources stronger than $5\,\mu$Jy.

We matched a simulated source to a cataloged component if (1) its position was within $\theta_{1/2}/2 = 3\farcs8$ of the cataloged position and (2) the catalog-to-true flux ratio satisfied $0.5 \le S_{\rm cat}/S_{\rm true} \le 2$. If there were two or more matches, only the strongest simulated source was matched with the cataloged component. If there were no simulated sources that satisfied these criteria, the cataloged component was rejected as spurious. The ten simulations yielded $\sim 1.6 \times 10^5$ matches. Only $\sim 0.5\%$ of the cataloged components had no simulated-source counterpart, for a catalog reliability $\approx 99.5\%$.

FndSou measures intensities relative to the image zero level. The DEEP2 interferometric image is insensitive to the smooth background of very faint radio sources. Our simulations of the radio sky brightness include such a background, so the average confusion $P(D)$ distribution from ten simulations of DEEP2 appears shifted by $\Delta D = +0.28\,\mu\mathrm{Jy\,beam^{-1}}$ compared with the $P(D)$ distribution of the real DEEP2 image. The final flux densities of components in the DEEP2 source catalog were corrected for the zero-level offset by subtracting $0.28\,\mu\mathrm{Jy\,beam^{-1}}$ from the peak flux densities reported by FndSou.

4.2. *DEEP2 Catalog Position Uncertainties*

The random position errors of DEEP2 source components are dominated by non-Gaussian confusion errors which are difficult to calculate analytically. Instead we estimated the random position errors from the differences $\Delta\alpha$, $\Delta\delta$ between the cataloged and "true" input positions of source components in our ten simulations. The normalized probability distributions $P(\Delta)$ are shown separately for right ascension α (red histogram) and declination δ (blue histogram) in Figure 6. The distributions of $\Delta\alpha$ and $\Delta\delta$ are indistinguishable, as expected for a circular PSF. Also as expected, the distributions of random positions errors are symmetrical about $\Delta = 0$ and have non-Gaussian tails—a Gaussian distribution would look like a parabola in the semilogarithmic Figure 6. The formal rms width of $P(\Delta)$ is dominated by these tails and is not a stable measure of the position error distribution. In a Gaussian distribution with rms σ, 68% of the sources would lie within the range $-\sigma < \Delta < +\sigma$, so we used the range of actual position offsets $\Delta\alpha \approx \Delta\delta$ and defined the "rms" position errors σ_α and σ_δ such that 68% of the components lie in the range $-\sigma_\alpha < \Delta\alpha < +\sigma_\alpha$ or $-\sigma_\delta < \Delta\delta < +\sigma_\delta$. The DEEP2 random position errors vary with component flux density S. For bins of width 0.2 in $\log(S)$ centered on $\log[S(\mu\mathrm{Jy})] = 1.1, 1.3, \ldots, 2.9$, we determined the distributions of position offsets $\Delta\alpha$ and $\Delta\delta$ in the ten simulations. Figure 7 shows $\sigma_\alpha \approx \sigma_\delta$ as a function of $\log(S)$.

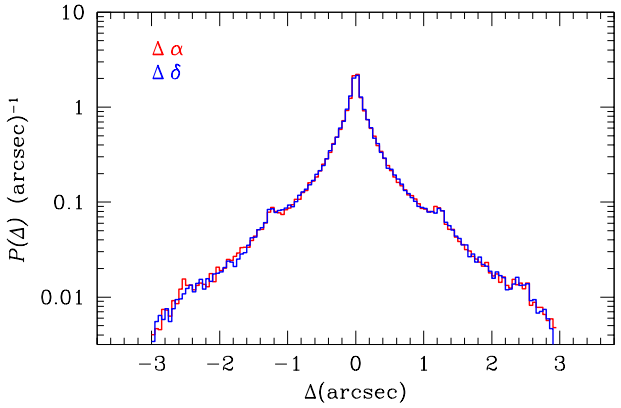

Figure 6. The distributions $P\,(\mathrm{arcsec})^{-1}$ of differences in right ascension $\Delta\alpha$ (red curve) and declination $\Delta\delta$ (blue curve) between the cataloged and "true" simulation positions for all sources with $S \ge 10\,\mu$Jy from ten simulated DEEP2 images. The small peaks at integer multiples of $\Delta = 1\farcs25$ pixel size are artifacts caused by our locating simulated sources only at the centers of $1\farcs25 \times 1\farcs25$ pixels.

The relationship betweeen this error limit and flux density is well described by a broken power-law of the form

$$\frac{\Delta\alpha}{\mathrm{arcsec}} = \frac{\Delta\delta}{\mathrm{arcsec}} = C\left[\left(\frac{S_*}{S}\right)^{R/2} + \left(\frac{S_*}{S}\right)^{R}\right]^{1/R}, \tag{11}$$

where the parameter R controls the sharpness of the break at $S = S_*$. A nonlinear least squares fit to Equation 11 yields $R = -11.97$, $C = 0.219$, and $S_* = 78.6\,\mu$Jy. As the catalogs were made for simulated images, there are no systematic position errors included in Equation 11. The dashed black curve in Figure 7

shows the random rms errors $\sigma_\alpha \approx \sigma_\delta$ as a function of component flux density.

To estimate the DEEP2 systematic position uncertainties and offsets, we selected the 268 strong components with calculated random errors $\sigma_\alpha = \sigma_\delta \leq 0\farcs05$ and used the NASA/IPAC Infrared Science Archive (IRSA) to find eight identifications with Gaia DR2 sources whose position errors are much smaller than $0\farcs05$. Their DEEP2 minus Gaia offsets have rms $\sigma_\alpha = \sigma_\delta = 0\farcs12 \pm 0\farcs04$, an insignificant mean offset $+0\farcs03 \pm 0\farcs04$ in right ascension, and a 3σ significant mean declination offset $+0\farcs12 \pm 0\farcs04$. We therefore added $-0\farcs12$ to our fitted DEEP2 declinations and added the $0\farcs12$ systematic position errors to the random errors in quadrature to get the total DEEP2 position shown by the continuous curve in Figure 7. The total position errors reported in the final component catalog (Table 2) reflect this quadrature sum and the corrected declinations.

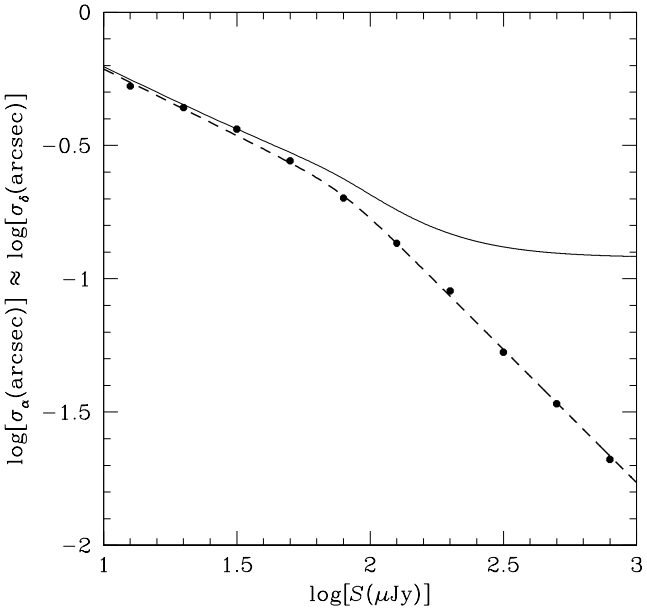

Figure 7. The simulation "rms" (defined as half the 68% confidence interval) random position error in either right ascension α and declination δ is shown as a function of flux density S by the points. The black dashed curve shows the best-fitting broken power-law from Equation 11. The total DEEP2 "rms" position uncertainties estimated by the quadrature sum of Equation 11 random errors and $0\farcs12$ systematic position errors are indicated by the solid curve.

4.3. *DEEP2 Catalog Flux-density Uncertainties*

We compared the flux densities calculated from the forced point-source fits of cataloged components in the ten simulated images with their "true" input flux densities. The distribution of these differences $\Delta S = S_{\rm cat} - S_{\rm true}$ is shown in Figure 8 for four flux density ranges: $10\,\mu{\rm Jy} < S < 10^{1.2} \sim 16\,\mu{\rm Jy}$, $10^{1.2}\,\mu{\rm Jy} < S < 10^{1.4} \sim 25\,\mu{\rm Jy}$, $10^{1.4}\,\mu{\rm Jy} < S < 10^{1.6} \sim 40\,\mu{\rm Jy}$, and $S > 10^{1.6}\,\mu{\rm Jy}$. The flux-density error distributions all peak near $\Delta S = 0\,\mu{\rm Jy}$ but have positive tails that grow with flux density because stronger components are able to obscure stronger confusing components.

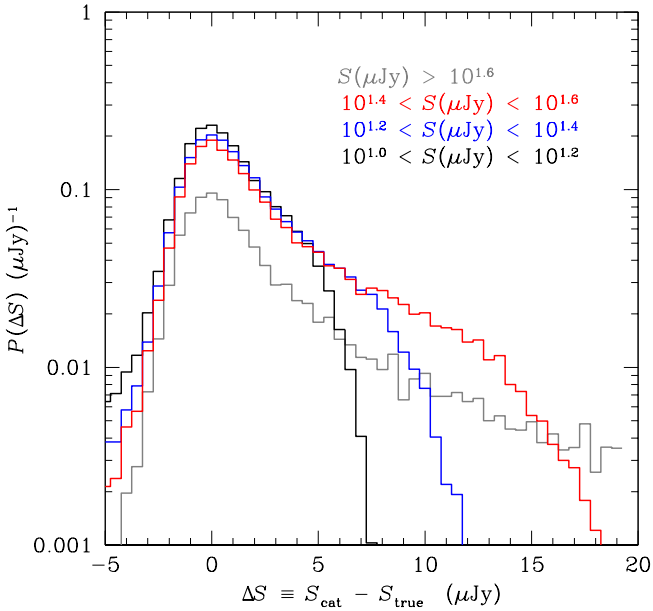

Figure 8. The differences $\Delta S = S_{\rm cat} - S_{\rm true}$ between the cataloged and "true" simulation flux density are shown for four catalog flux-density ranges: $10\,\mu{\rm Jy} < S < 10^{1.2} \sim 16\,\mu{\rm Jy}$ (black), $10^{1.2}\,\mu{\rm Jy} < S < 10^{1.4} \sim 25\,\mu{\rm Jy}$ (blue), $10^{1.4}\,\mu{\rm Jy} < S < 10^{1.6} \sim 40\,\mu{\rm Jy}$ (red), and $S > 10^{1.6}\,\mu{\rm Jy}$ (gray).

The fractional flux density errors σ_S/S were calculated for all ten catalogs of the simulated images in bins of width 0.2 dex centered on $\log[S\,(\mu{\rm Jy})] = 1.1, 1.3, \ldots, 2.9$ and are shown in Figure 9. In the ideal case of uncorrelated Gaussian noise, high signal-to-noise S/σ_S, and a circular Gaussian beam of FWHM $\theta_{1/2}$, Equation 21 of Condon (1997) gives

$$\frac{\sigma_S}{S} = \sqrt{8\ln 2}\left(\frac{\sigma_\alpha}{\theta_{1/2}}\right) = \sqrt{8\ln 2}\left(\frac{\sigma_\delta}{\theta_{1/2}}\right), \qquad (12)$$

so for either α or δ,

$$\log\left(\frac{\sigma_S}{S}\right) = \log(8\ln 2)/2 + \log(\sigma_\alpha) - \log(\theta_{1/2})$$
$$= \log(\sigma_\alpha) - 0.51, \qquad (13)$$

for $\theta_{1/2} = 7\farcs6$. This gives conservative flux-density fitting errors. To them we add in quadrature a 2% uncer-

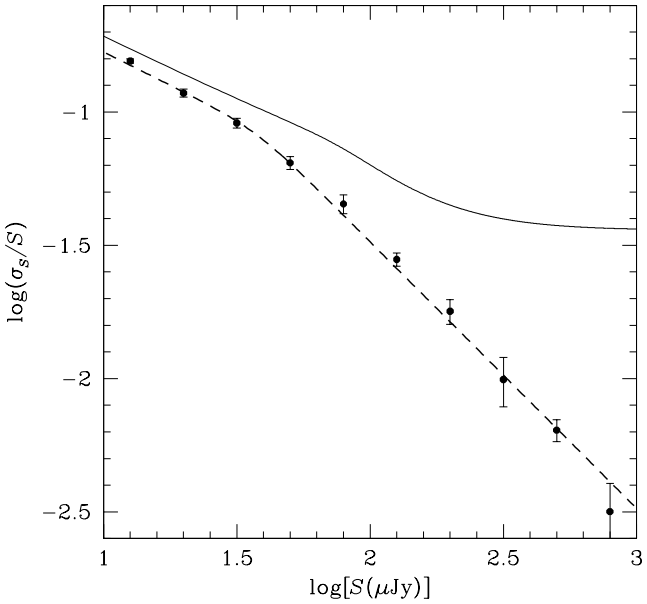

Figure 9. The random fractional flux density errors per catalog flux density bin was calculated as the narrowest range of the distribution containing 68% of the sources (black points). The dashed line shows a broken power-law fit to thsee calculated errors. The total component error σ_S/S) from Equation 14 is shown as the solid black curve.

tainty for telescope pointing errors and primary attenuation uncertainty inside the primary beam half-power circle plu a 3% for the absolute flux-density uncertainty of the gain calibrator PKS B1934−638 (Mauch et al. 2020) to get the total fractional uncertainty

$$\frac{\sigma_S}{S} = \left(8 \ln 2 \frac{\sigma_\alpha^2}{\theta_{1/2}^2} + 0.036^2 \right)^{1/2} . \quad (14)$$

The fractional flux density errors calculated from Equation 14 are shown by the solid black curve in Figure 9. This method yields more conservative error estimates than directly fitting the measured flux differences from the simulated images with a broken power law for flux densities $\log S < 2.5$ when these measured differences are added in quadrature with the cumulative calibration uncertainties (shown as the dotted line in Figure 9).

The ten simulated images were corrected for primary beam attenuation before the catalog was created, so the noise contribution increases distance r from the pointing center as

$$\sigma_{\rm n}(r) = \frac{0.57\,\mu{\rm Jy\,beam}^{-1}}{a(r)}, \quad (15)$$

where

$$a(r) = \exp\left(-4 \ln 2 \frac{r^2}{\Theta_{1/2}^2} \right), \quad (16)$$

Table 2. The 1.266 GHz DEEP2 Component Catalog

Right Ascension (J2000)	Declination (J2000)	S(1.266 GHz) (μJy)	Group Code
04:08:34.781 ± 0.170	−79:51:43.08 ± 0.45	20.0 ± 2.1	···
04:08:34.897 ± 0.089	−80:20:26.14 ± 0.22	87.2 ± 5.3	G09
04:08:34.956 ± 0.166	−79:35:02.48 ± 0.45	20.0 ± 2.2	···
04:08:34.986 ± 0.160	−80:24:19.47 ± 0.40	25.5 ± 2.5	···
04:08:35.066 ± 0.051	−79:47:01.95 ± 0.13	278.0 ± 10.5	···

Note—Table 2 is published in its entirety in machine-readable format. A portion is shown here for guidance regarding its form and content. The quoted uncertainties are similar to rms errors in that they encompass 68% of the sources but are insensitive to the long tails of confusion-limited error distributions. There are 35 multicomponent sources labeled by their component group numbers G01 through G35, as described in Section 4.4.

is the primary beam attenuation. The simulation placed sources in the sky randomly but uniformly, so we subtracted the average noise variance within the half-power circle $\langle \sigma_{\rm n} \rangle = 0.824\,\mu{\rm Jy\ beam}^{-1}$ from the total average flux density variance calculated from Equation 14. We added back the distance-depndent rms noise variance to get a better estimate of errors on the individual source flux densities at various distances from the pointing center.

4.4. *Multicomponent Sources*

We visually inspected the DEEP2 image and found 35 groups of components that appear to comprise multicomponent radio sources. We labeled these components by their group numbers G01 to G35. For extended sources well approximated by a collection of Gaussian components, we summed the individual component flux densities to determine the source flux density. For sources containing diffuse emission regions, we estimated the flux density of such regions by directly summing over the pixel brightness distribution. Table 3 lists the 35 multicomponent sources, the number of components in each source group, our best estimate of the source core position, and the source flux density. Figure 10 shows the contour map of multicomponent source G01 with crosses marking the positions of its three components. Similar contour maps of all multicomponent sources appear in the Appendix.

5. DEEP2 DIRECT SOURCE COUNTS

We counted DEEP2 sources in bins of width 0.2 dex centered on 1.266 GHz flux densities $\log[S({\rm Jy})] = -4.9, -4.7, \ldots, -2.5$. Component groups comprising an extended source were counted as a single source whose

Table 3. DEEP2 Multicomponent sources

Group Code	N	Right Ascension (J2000)	Declination (J2000)	S (μJy)
G01	3	04:00:47.04	−79:51:31.4	817
G02	3	04:01:31.81	−79:59:08.6	159
G03	8	04:03:54.19	−80:08:49.1	757
G04	4	04:04:05.81	−79:58:56.2	709
G05	3	04:04:14.84	−79:56:21.5	13536
G06	3	04:06:15.50	−80:10:57.5	2742
G07	3	04:06:26.05	−79:38:01.0	168
G08	7	04:06:27.83	−80:18:48.0	19200
G09	14	04:08:42.38	−80:20:40.9	885
G10	12	04:08:47.70	−80:24:02.4	1569
G11	5	04:11:32.60	−79:48:41.3	766
G12	3	04:11:38.97	−79:48:17.5	2867
G13	11	04:11:59.21	−80:14:54.8	1422
G14	7	04:12:16.93	−79:46:33.2	6772
G15	5	04:12:32.00	−79:34:36.4	509
G16	8	04:13:24.93	−79:49:21.2	5455
G17	9	04:13:41.22	−79:46:34.9	6680
G18	4	04:13:58.03	−79:42:19.2	1369
G19	18	04:14:17.93	−80:11:38.4	5455
G20	5	04:14:58.85	−80:29:08.4	1261
G21	3	04:16:10.11	−80:03:31.9	169
G22	6	04:16:23.34	−80:20:54.5	4699
G23	3	04:16:47.09	−79:48:50.3	54268
G24	5	04:16:58.32	−79:54:46.2	1953
G25	9	04:17:02.19	−80:12:33.9	6115
G26	3	04:17:06.86	−79:51:28.6	3682
G27	7	04:18:58.15	−79:51:23.5	1603
G28	10	04:19:10.77	−80:30:32.4	3051
G29	4	04:20:03.10	−80:27:11.3	2769
G30	14	04:22:05.41	−80:03:30.1	10882
G31	5	04:23:19.81	−79:51:10.6	11408
G32	8	04:25:02.63	−80:14:15.9	26271
G33	6	04:25:18.38	−79:52:22.3	15983
G34	9	04:25:51.5	−79:54:38	731
G35	8	04:26:07.75	−80:09:23.7	766

flux density is the sum of its individual component flux densities. For the few extended sources with diffuse emission regions, we estimated the flux densities of these regions by directly summing over their pixel brightness distributions.

Sources near the catalog lower limit $S(1.266\,\mathrm{GHz}) = 10\,\mu$Jy may be biased up by confusion or biased low and missed entirely. We estimated the effects of confusion on the direct source counts by comparing the measured counts in the ten simulated images with the "true" input counts. Their differences in each flux-density bin were calculated individually for the ten simulations. We added the mean differences Δ in $\log[S^2 n(S)]$ from the simulations to the raw DEEP2 counts to yield more accurate counts of radio sources with $-5.0 < \log[S(\mathrm{Jy})] < -2.5$.

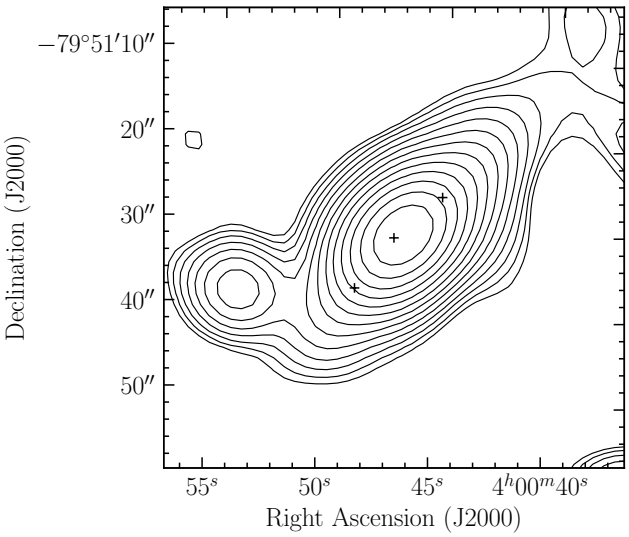

Figure 10. Multicomponent source G01. Contour levels $\pm 5\,\mu\mathrm{Jy\,beam^{-1}} \times 2^0, 2^{1/2}, 2^1, \ldots$ are plotted. Crosses mark the three components comprising this source.

Table 4 shows the $\nu = 1.266\,\mathrm{GHz}$ corrected counts based on the 17,350 DEEP2 sources with $S > 10\,\mu$Jy located within the $\Omega = \pi\Theta_{1/2}^2/4 \approx 3.182 \times 10^{-4}\,\mathrm{sr}$ half-power circle of the primary beam. For the 13 flux-density bins of width 0.2 in $\log(S)$, Column 1 lists the bin center $\log[S(\mathrm{Jy})]$ and column 2 lists the number N_{bin} of sources in the bin. The corrections Δ in column 3 were added to the values of $\log[S^2 n(S)\,(\mathrm{Jy\,sr^{-1}})]$ in column 4. Columns 5 and 6 are the rms positive and negative uncertainties in $\log[S^2 n(S)]$. These uncertainties are the quadratic sum of the Poisson uncertainties in samples of size N_{bin}, the count correction uncertainties which we conservatively estimate to be $\Delta/2$, and a 3% overall flux-density scale uncertainty.

6. NVSS SOURCE COUNTS

The 1.4 GHz NRAO VLA Sky Survey (NVSS) (Condon et al. 1998) imaged the entire sky north of J2000 $\delta = -40°$ with $\theta_{1/2} = 45''$ FWHM resolution and $\sigma_{\mathrm{n}} \approx 0.45\,\mathrm{mJy\,beam^{-1}}$ rms noise. The NVSS catalog lists source components as Gaussian fits to significant peaks in the NVSS images. From it we selected the 1117067 components with $S \geq 2.5$ mJy in the $\Omega \approx 7.016$ sr solid angle bounded by absolute Galactic latitude $|b| \geq 20°$ and J2000 declination $\delta \geq -40°$.

Table 4. DEEP2 1.266 GHz direct source counts

log[S(Jy)]	$N_{\rm bin}$	Δ	log[$S^2n(S)$ (Jy sr^{-1})]	
−4.90	5504	+0.054	2.730	+0.028 −0.029
−4.70	4460	+0.020	2.801	+0.017 −0.018
−4.50	3010	−0.022	2.788	+0.018 −0.019
−4.30	1998	−0.027	2.802	+0.020 −0.021
−4.10	1053	−0.034	2.716	+0.025 −0.027
−3.90	559	−0.035	2.639	+0.029 −0.031
−3.70	289	−0.028	2.563	+0.031 −0.034
−3.50	126	−0.012	2.423	+0.040 −0.044
−3.30	72	−0.011	2.366	+0.050 −0.057
−3.10	46	−0.005	2.393	+0.061 −0.072
−2.90	24	−0.006	2.305	+0.082 −0.102
−2.70	15	−0.001	2.317	+0.101 −0.132
−2.50	18	−0.009	2.587	+0.093 −0.119

Table 5. NVSS 1.4 GHz source counts

log[S(Jy)]	$N_{\rm bin}$	log[$S^2n(S)$ (Jy sr^{-1})]	
−2.50	350531	2.475	+0.030 −0.030
−2.30	217350	2.498	+0.019 −0.019
−2.10	161525	2.598	+0.015 −0.015
−1.90	120302	2.676	+0.014 −0.014
−1.70	90072	2.743	+0.013 −0.013
−1.50	63706	2.793	+0.013 −0.013
−1.30	43803	2.831	+0.013 −0.013
−1.10	29035	2.849	+0.013 −0.013
−0.90	18094	2.844	+0.013 −0.013
−0.70	10891	2.822	+0.013 −0.013
−0.50	5950	2.757	+0.014 −0.014
−0.30	3089	2.670	+0.015 −0.015
−0.10	1477	2.551	+0.017 −0.017
+0.10	718	2.434	+0.021 −0.021
+0.30	303	2.247	+0.028 −0.028
+0.50	143	2.137	+0.038 −0.038
+0.70	51	1.995	+0.080 −0.080
+0.90	15	1.739	+0.140 −0.140
+1.10	6	1.523	+0.214 −0.229
+1.30	3	1.285	+0.295 −0.341

The NVSS catalog reports flux densities rounded to the nearest multiple of 0.1 mJy. For example, all NVSS components with fitted flux densities $2.45 \le S(\mathrm{mJy}) < 2.55$ are listed as having $S = 2.5$ mJy. We separated the NVSS components into flux-density bins of nearly constant width 0.2 in $\log(S)$ whose exact boundaries $S_{\rm min}$ and $S_{\rm max}$ are midway between multiples of 0.1 mJy. Thus the lowest flux-density bin covers $2.45 \le S(\mathrm{mJy}) < 3.95$ and includes all NVSS components listed with $S(\mathrm{mJy}) = 2.5, 2.6, 2.7, \ldots, 3.9$. The first column of Table 5 lists the bin centers, the second lists the numbers $n_{\rm bin}$ of components in each bin, and the third column shows the brightness-weighted counts $\log[S^2n(S)]$ at $\log[S(\mathrm{Jy})] = -2.5, -2.3, \ldots, +1.3$. The fourth and fifth columns are the total rms uncertainties in $\log[S^2n(S)]$.

Complex radio sources significantly more extended than the 45″ FWHM NVSS restoring beam may be represented by two or more catalog components, and such large multicomponent sources are more common at flux densities $S \gtrsim 1$ Jy. To estimate the fraction of components comprising strong extended sources, we compared the NVSS component catalog with the low-resolution 1.4 GHz Bridle et al. (1972) catalog of 424 sources having $S \ge 1.7$ Jy and equivalent angular diameters $\phi \lesssim 10'$ in the area defined by $-5° < \delta < +70°$, $|b| > 5°$. We combined NVSS components within $\sim 5'$ of each Bridle et al. (1972) source, after excluding those that appeared to be unrelated background sources. In the six flux-density bins centered on $\log[S(\mathrm{Jy})] = +0.3$ through +1.3, grouping NVSS components into sources changed the brightness-weighted source count $\log[S^2n(S)(\mathrm{Jy\ sr^{-1}})]$ by −0.013, +0.013, +0.109, +0.193, +0.133, and 0.000, respectively.

The differential source count $n(S)$ is a rapidly declining function of flux density, so simply counting the number of sources in each fairly wide flux-density bin throws away flux-density information and can bias the resulting estimate of $n(S)$. If $n(S)\,dS$ is the number of sources per steradian with flux densities between S and $S + dS$ and $\eta(S)\,d\ln(S)$ is the number per steradian with flux densities between S and $S + d\ln(S)$, then $n(S)dS = \eta(S)\,d\ln S$ and $n(S) = \eta(S)/S$. We added the flux density of each source into its bin of logarithmic width $\Delta \approx \mathrm{dex}(0.2)$ to calculate the more nearly constant quantity

$$S^2n(S) = S\eta(S) = \left[\frac{1}{\Omega \ln(\Delta)}\right] \sum_{i=1}^{n_{\rm bin}} S_i \qquad (17)$$

directly.

Finally, counts in the faintest bins must be corrected for population-law bias (Murdoch et al. 1973): faint sources outnumber strong sources, so noise moves more faint sources into a bin than it moves strong sources out. We used their Table 2 and the cumulative source-count approximation $N(>S) \equiv \int_S^\infty n(S)\,dS \propto S^{-1}$ for $S \gtrsim 2.5$ mJy to calculate the required corrections to $\log[S^2n(S)]$. They are −0.030, −0.012, and −0.004 in bins centered on $\log[S(\mathrm{Jy})] = -2.5$, −2.3, and −2.1, respectively.

The rms statistical uncertainty in $S^2n(S)$ for each bin with $n_{\rm bin} \gg 1$ is

$$\sigma_{\rm stat} \approx \left[\frac{1}{\Omega \ln(\Delta)}\right] \left(\sum_{i=1}^{n_{\rm bin}} S_i^2\right)^{1/2} . \quad (18)$$

There are only $n_{\rm bin} = 6$ sources in the $\log[S(\mathrm{Jy})] = +1.1$ bin and $n_{\rm bin} = 3$ sources in the $\log[S(\mathrm{Jy})] = +1.3$ bin, so we replaced their rms statistical errors in $\log[S^2n(S)]$ by the Gehrels (1986) 84% confidence-level errors $+0.203, -0.219$ and $+0.295, -0.341$, respectively. To these statistical uncertainties we added quadratically the 3% error in $S^2n(S)$ caused by the 3% NVSS flux-density scale uncertainty (Condon et al. 1998) and systematic uncertainties equaling half the corrections for component grouping and population-law bias.

7. SUMMARY

Figure 4 shows our 1.4 GHz differential source counts with traditional static-Euclidean weighting $S^{5/2}n(S)$ and with brightness weighting $S^2n(S)$. Counts from $S = 0.25\,\mu$Jy to $S = 10\,\mu$Jy were derived statistically from the DEEP2 confusion $P(D)$ distribution extracted from solid angle $\Omega = 1.85 \times 10^{-5}$ sr. Individual sources uniformly covering solid angle $\Omega = 3.182 \times 10^{-4}$ sr $= 1.04\,\mathrm{deg}^2$ between $10\,\mu$Jy and $2.5\,\mu$J were counted directly, as were NVSS sources above 2.5 mJy in solid angle $\Omega = 7.016$ sr (0.56 of the sky). Together these counts span the eight decades in flux density from $\log[S(\mathrm{Jy})] = -6.6$ to $\log[S(\mathrm{Jy})] = +1.4$. Their largest fractional uncertainties are caused by the rms noise $\sigma_{\rm n} = 0.57 \pm 0.01\,\mu\mathrm{Jy\,beam}^{-1}$ and finite resolution $\theta_{1/2} = 7\farcs6$ just above $S = 0.25\,\mu$Jy, by statistical fluctuations in the small numbers of sources in the $\Omega = 1.04\,\mathrm{deg}^{-2}$ DEEP2 half-power circle between 0.5 mJy and 2.5 mJy, and by cosmic variance in the NVSS counts covering $\Omega = 7.016$ sr above $S \approx 3$ Jy.

Figure 11 compares our 1.4 GHz direct counts (black points) of sources fainter than 10 mJy with those of Hopkins et al. (2003) (blue points), Prandoni et al. (2018) (red points), Heywood et al. (2020) (magenta points), and the Smolčić et al. (2017) 3 GHz counts converted to 1.4 GHz assuming the median spectral index is $\langle\alpha\rangle = -0.7$. The latter counts have small ($\sigma \sim 10\%$) uncertainties because they are based on the large (10,830 sources) noise-limited (median $\sigma_{\rm n} = 2.3\,\mu$Jy beam at 3 GHz) VLA-COSMOS catalog. They are $\sim 20\% \sim 2\sigma$ lower than the other counts, possibly because resolution corrections for the small ($\theta_{1/2} = 0\farcs75$) VLA COSMOS beam were insufficient or the median spectral index of μJy sources is more negative than the assumed -0.7 — correcting from 3 GHz to 1.4 GHz with $\alpha = -0.8$ would halve the difference. In any case, the agreement among all of these μJy source counts is much better than in the past (Heywood et al. 2013), suggesting that the large earlier discrepancies were caused by observational and analysis errors, not by surprisingly strong source clustering.

7.1. *Resolving the AGN and SFG backgrounds*

The 1.4 GHz brightness-weighted counts $S^2n(S)$ shown in Figure 4 have two broad peaks. The peak $S \sim 0.1$ Jy is dominated by AGNs and the peak at $S \sim 3 \times 10^{-5}$ Jy by SFGs. If the counts below $S = 0.25\,\mu$Jy do not exceed the extrapolation with slope $d\log[S^2n(S)]/d\log(S) = +0.5$, sources stronger $S = 0.25\,\mu$Jy resolve $> 99\%$ of the AGN contribution $\Delta T_{\rm b} \approx 0.06$ K to the sky brightness temperature and $> 96\%$ of the $\Delta T_{\rm b} \approx 0.04$ K SFG contribution. Thus most of the stars in the universe were formed in SFGs stronger than $0.25\,\mu$Jy. For example, our fairly typical Galaxy currently has 1.4 GHz spectral luminosity $L_\nu \approx 2.5 \times 10^{21}\,\mathrm{W\,Hz}^{-1}$. With $10\times$ luminosity evolution (Madau & Dickinson 2014), it would be a $1.2\,\mu$Jy source around "cosmic noon" at $z \sim 2$ and a $0.25\,\mu$Jy source even at $z = 4$.

7.2. *$P(D)$ limits on "new" source populations*

Can one or more "new" populations of radio sources fainter than $0.25\,\mu$Jy make comparable contributions to the sky brightness at 1.4 GHz? The ARCADE 2 instrument measured the absolute sky temperature at frequencies from $\nu = 3 - 90$ GHz, and Fixsen et al. (2011) reported finding an excess power-law brightness temperature

$$\left(\frac{T_{\rm b}}{\rm K}\right) = (24.1 \pm 2.1) \left(\frac{\nu}{\nu_0}\right)^{-2.599 \pm 0.036} \quad (19)$$

from 22 MHz to 10 GHz, where $\nu_0 = 310$ MHz. Removing the contribution from known populations of extragalactic sources leaves

$$\left(\frac{\Delta T_{\rm b}}{\rm K}\right) = (18.4 \pm 2.1) \left(\frac{\nu}{\nu_0}\right)^{-2.57 \pm 0.05} , \quad (20)$$

(Seiffert et al. 2011). Possible explanations for this large excess fall into three categories: 1) the excess was overestimated owing to the limited sky coverage of ARCADE 2 and the zero-point levels of low frequency radio maps may be inaccurate, 2) the excess is primarily smooth emission from our Galaxy, 3) the excess is primarily extragalactic, making it the only photon background that does not agree with published source counts dominated by radio galaxies and star-forming galaxies. Vernstrom

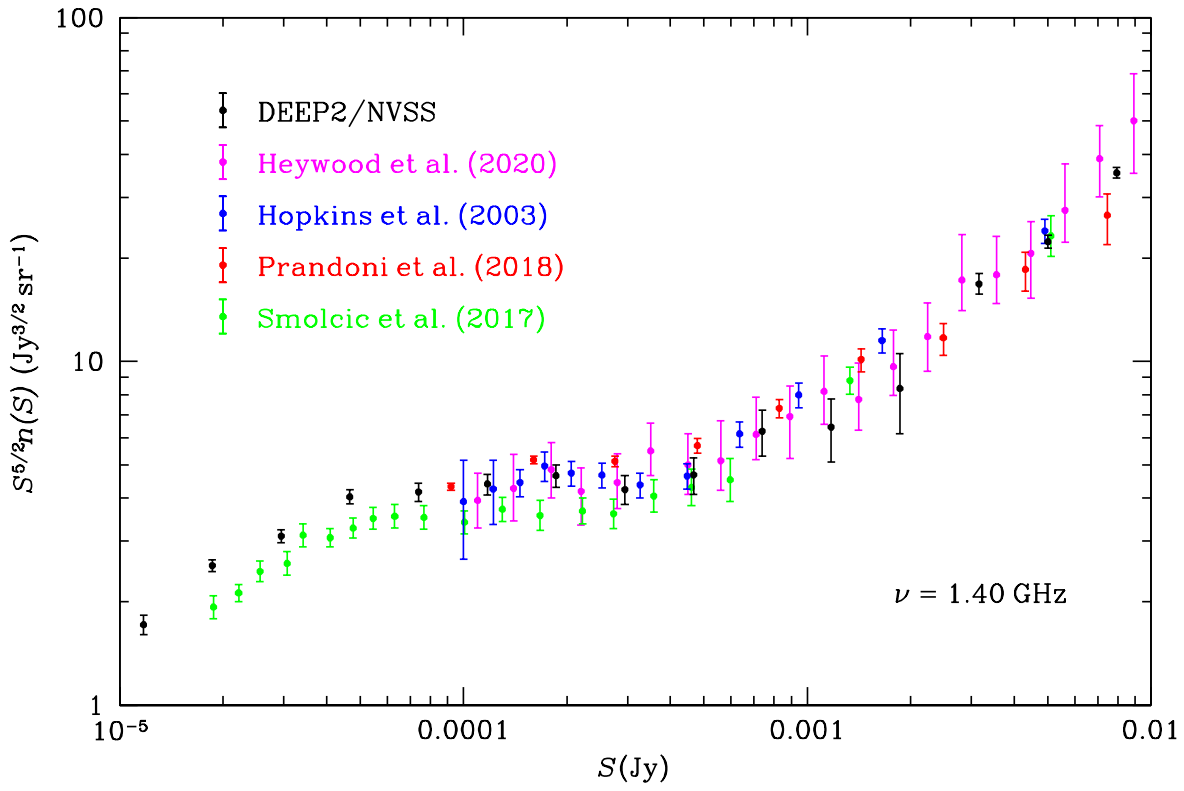

Figure 11. The 1.4 GHz differential source counts between 10 μJy and 10 mJy are shown with the traditional static Euclidean normalization $S^{5/2}n(S)$. The black data points show the DEEP2 source counts below $S = 0.0025$ Jy (Section 4) and the NVSS counts (Section 6 at higher flux densities. The magenta data points are from Heywood et al. (2020), the blue data points are from Hopkins et al. (2003), and the red data points are from Prandoni et al. (2018). The green data points are based on the Smolčić et al. (2017) 3 GHz counts converted to 1.4 GHz with a spectral index $\alpha = -0.7$.

et al. (2011) and Seiffert et al. (2011) explored the possibility of a new source population contributing an extra "bump" to the source counts at flux densities $< 10\,\mu$Jy. In order to match the ARCADE 2 excess background, this hypothetical new population must add $\Delta T_b \sim 0.4$ K to the sky brightness at 1.4 GHz. Condon et al. (2012) showed that the brightness-weighted counts $S^2n(S)$ of this new population must peak at flux densities below $S_{1.4\,\mathrm{GHz}} = 0.1\,\mu$Jy to be consistent with their observed $P(D)$ distribution.

The MeerKAT correlation interferometer used to make the DEEP2 image does not respond to backgrounds smooth on angular scales $\gg \theta_{1/2} = 7\farcs6$, and the resolution of ARCADE 2 is too coarse to detect individual $< 0.1\,\mu$Jy sources, so there is actually no *observational* tension between our results in Section 7.1 and the ARCADE 2 background. However, the DEEP2 $P(D)$ distribution can set a lower limit to the *number* of faint sources not much larger than $\theta_{1/2} = 7\farcs6 \approx 50$ kpc in the redshift range $0.5 < z < 5$ that can produce a $\Delta T_b \sim 0.4$ K background smooth enough to be consistent with the DEEP2 $P(D)$ distribution. Very numerous faint sources contribute a nearly Gaussian $P(D)$ distribution similar to the instrumental noise distribution. A source population with rms confusion not much larger than $\sigma_c \approx (0.58^2 - 0.57^2)^{1/2}\,\mu\mathrm{Jy\,beam}^{-1} \sim 0.1\,\mu\mathrm{Jy\,beam}^{-1}$ is consistent with the uncertainty in the measured DEEP2 rms noise. Figure 12 plots the brightness-weighted source counts $S^2n(S)$ as a function of $\log(S)$. The two broad peaks corresponding to star-forming galaxies and AGN are well represented by the approximation (Condon et al. 2012) $\log[S^2n(S)] \approx a - b[\log(S) - \log(S_{\mathrm{pk}})]^2$ or

$$S^2n(S) \approx A \exp\left\{-4\ln(2)\frac{[\log(S) - \log(S_{\mathrm{pk}})]^2}{\phi^2}\right\}, \quad (21)$$

where ϕ is the logarithmic FWHM and S_{pk} is the flux density of the $S^2n(S)$ peak; $\log(S_{\mathrm{pk}}) \sim -5$ and $\log(S_{\mathrm{pk}}) \sim -1$ for SFGs and AGNs, respectively, while both populations are well described by $\phi = 2$. Inserting Equation 21 into Equation 1 and integrating over flux density determines the peak amplitude A for FWHM ϕ

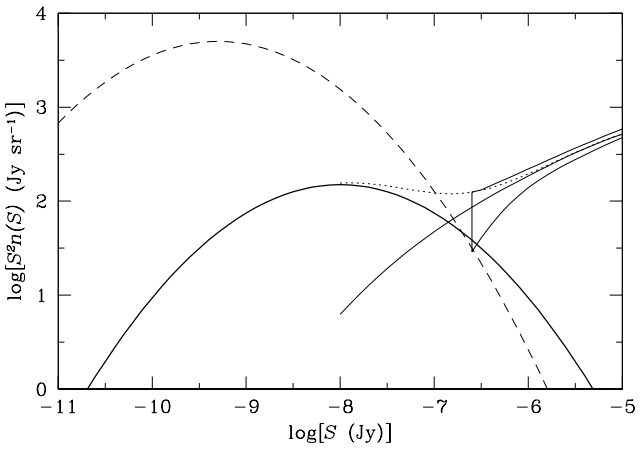

Figure 12. Source counts at 1.4 GHz consistent with the DEEP2 $P(D)$ distribution are shown by the thin black line surrounded by its $\pm1\sigma$ error region. A hypothetical new population with logarithmic FWHM $\phi = 2$ and $A = 150$ located at $\log(S_{\rm pk}) = -8$ (thick black parabola) is consistent with DEEP2, but it contributes only 10 mK to the radio source background. A hypothetical population contributing the necessary 0.4 K to agree with the background measured by ARCADE 2 must have $A \approx 5000$ and $S^2n(S)$ peaking at $S_{\rm pk} \leq 0.5$ nJy (black dashed parabola) to remain consistent with our DEEP2 $P(D)$ observation.

for a new population adding $\Delta T_{\rm b}$ to the total sky brightness:

$$A\phi = \frac{4k_{\rm B}\nu^2}{\ln(10)c^2}\left[\frac{\ln(2)}{\pi}\right]^{1/2}\Delta T_{\rm b}. \quad (22)$$

Equation 22 is valid for any count peak flux density $S_{\rm pk}$. Because $\Delta T_{\rm b}$ fixes the product $A\phi$, a new population with $T_{\rm b}$ either has a small number of sources N with a narrow FWHM ϕ but large amplitude A, or a broad peak ϕ with a larger number of sources per square arcmin and a fainter peak flux density.

The known AGN and SFG populations are well characterized by Gaussians of FWHM $\phi = 2$, so we assumed $\phi = 2$ for the hypothetical new population. In order to explain the excess $\Delta T_{\rm b} = 0.4$ K, the amplitude of this population must be $A \sim 5000$ Jy sr^{-1}.

For any $S_{\rm pk}$ we can find the maximum value of A that is consistent with the DEEP2 $P(D)$. Inserting a new population of sources with $\phi = 2$ and $\log(S_{\rm pk}) = -8$, we ran DEEP2 image simulations starting at $\log[S({\rm Jy})] = -10$ for increasing values of A in steps of 10 from $A = 0$. They were repeated for $\langle\sigma_{\rm n}\rangle = 0.56\,\mu$Jy beam^{-1} and $0.58\,\mu$Jy beam^{-1} in addition to the measured rms noise averaged throughout the $P(D)$ region of radius 500″, $\langle\sigma_{\rm n}\rangle = 0.57\mu$Jy beam^{-1}. Having run a minimum of 50 iterations, we determined the χ^2 value of each simulated $P(D)$ distribution (containing the new population of amplitude A) to the observed $P(D)$. The value of A such that 16% of the simulations had $\chi^2 < \chi^2_0$ is the 1σ upper limit to the amplitude A that is consistent with our observed $P(D)$.

For rms noise values $\sigma_n = 0.56$ and $0.57\,\mu$Jy beam^{-1} the maximum amplitude consistent with the observed DEEP2 $P(D)$ distribution is $A \approx 65$. Simulations assuming rms noise $\sigma_{\rm n} = 0.55\,\mu$Jy beam^{-1} allow $A < 150$. The final 1σ upper bound on the counts of nJy sources is the combination of Equation 4 and the curve representing the sum of the new population and the measured counts from DEEP2 (dotted curve in Figure 12).

Figure 12 shows the brightness-weighted source counts for the hypothetical population with $A = 150, \phi = 2$, and $S_{\rm pk} = 10$ nJy as the thicker black curve. That new population adds only $\Delta T_{\rm b} \sim 0.01$ K to the total radio source background at 1.4 GHz, yet it must contain at least 3,000 sources per arcmin^2, exceeding by a factor of 30 the sky density of galaxies brighter than $m_{\rm AB} + 29$, the magnitude of the Large Magellanic Cloud at redshift $z = 2$) in the Hubble Ultra Deep Field (Beckwith et al. 2006).

A hypothetical new population contributing the full 0.4 K ARCADE 2 excess background is consistent with the narrow DEEP2 $P(D)$ distribution only if $\log(A) \approx 3.7$, the sources are randomly distributed on the sky, and $S_{\rm pk} < 0.5$ nJy at 1.4 GHz. as indicated by the dashed parabola in Figure 12). This upper limit to $S_{\rm pk}$ is a factor of ten lower than the Condon et al. (2012) limit and more strongly excludes a bright population of numerous faint sources that cluster like galaxies or parts of galaxies.

ACKNOWLEDGMENTS

The MeerKAT telescope is operated by the South African Radio Astronomy Observatory, which is a facility of the National Research Foundation, an agency of the Department of Science and Technology. The National Radio Astronomy Observatory is a facility of the National Science Foundation operated by Associated Universities, Inc. This material is based upon work supported by the National Science Foundation Graduate Research Fellowship under Grant No. DDGE-1315231.

Facilities: Gaia, IRSA, MeerKAT

REFERENCES

Beckwith, S. V. W., Stiavelli, M., Koekemoer, A. M., et al. 2006, AJ, 132, 1729

Benn, C. R., & Wall, J. V. 1995, MNRAS, 272, 678

Béthermin, M., Wu, H.-Y., Lagache, G., et al. 2017, A&A, 607, A89

Bridle, A. H., Davis, M. M., Fomalont, E. B., & Lequeux, J. 1972, AJ, 77, 405

Condon, J. J. 1974, ApJ, 188, 279

—. 1984, ApJ, 287, 461

—. 1997, PASP, 109, 166

Condon, J. J., Cotton, W. D., Greisen, E. W., et al. 1998, AJ, 115, 1693

Condon, J. J., & Matthews, A. M. 2018, PASP, 130, 073001

Condon, J. J., Cotton, W. D., Fomalont, E. B., et al. 2012, ApJ, 758, 23

Cotton, W. D. 2008, PASP, 120, 439

Cotton, W. D., Condon, J. J., Kellermann, K. I., et al. 2018, ApJ, 856, 67

Fixsen, D. J., Kogut, A., Levin, S., et al. 2011, ApJ, 734, 5

Gehrels, N. 1986, ApJ, 303, 336

Heywood, I., Hale, C. L., Jarvis, M. J., et al. 2020, arXiv e-prints, arXiv:2006.08551

Heywood, I., Jarvis, M. J., & Condon, J. J. 2013, MNRAS, 432, 2625

Hopkins, A. M., Afonso, J., Chan, B., et al. 2003, AJ, 125, 465

Jauncey, D. L. 1968, ApJ, 152, 647

Madau, P., & Dickinson, M. 2014, ARA&A, 52, 415

Mauch, T., Cotton, W. D., Condon, J. J., et al. 2020, ApJ, 888, 61

Morrison, G. E., Owen, F. N., Dickinson, M., Ivison, R. J., & Ibar, E. 2010, ApJS, 188, 178

Murdoch, H. S., Crawford, D. F., & Jauncey, D. L. 1973, ApJ, 183, 1

Owen, F. N. 2018, ApJS, 235, 34

Prandoni, I., Guglielmino, G., Morganti, R., et al. 2018, MNRAS, 481, 4548

Scheuer, P. A. G. 1957, Proceedings of the Cambridge Philosophical Society, 53, 764

Seiffert, M., Fixsen, D. J., Kogut, A., et al. 2011, ApJ, 734, 6

Smolčić, V., Novak, M., Bondi, M., et al. 2017, A&A, 602, A1

Vernstrom, T., Scott, D., & Wall, J. V. 2011, MNRAS, 415, 3641

APPENDIX

A. MULTICOMPONENT SOURCE CONTOUR MAPS

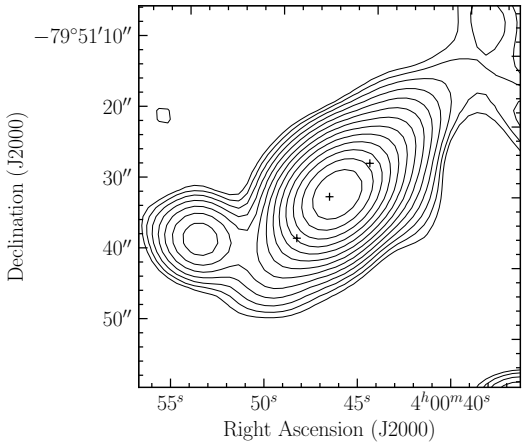

G01: 04:00:47 −79:51:31

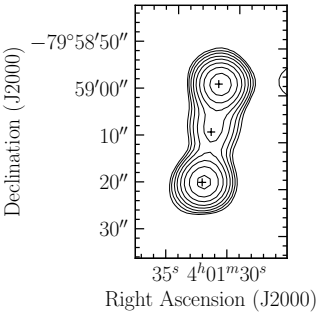

G02: 04:01:31.81 −79:59:08.5

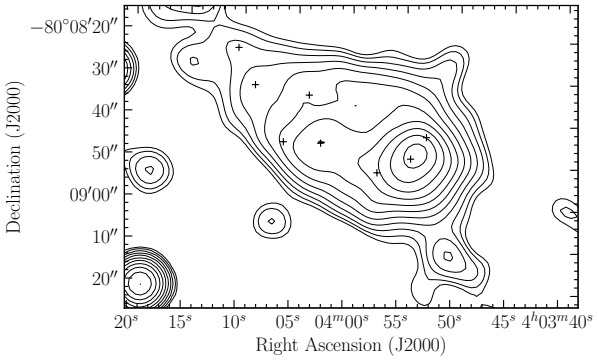

G03: 04:03:54.9 −80:08:49.0

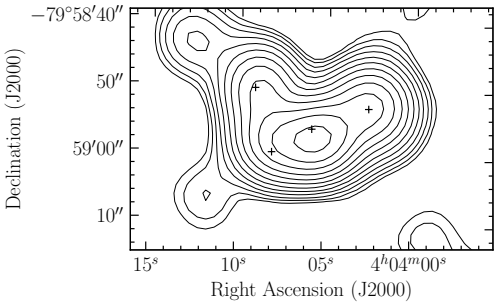

G04: 04:04:05.81 −79:58:56.1

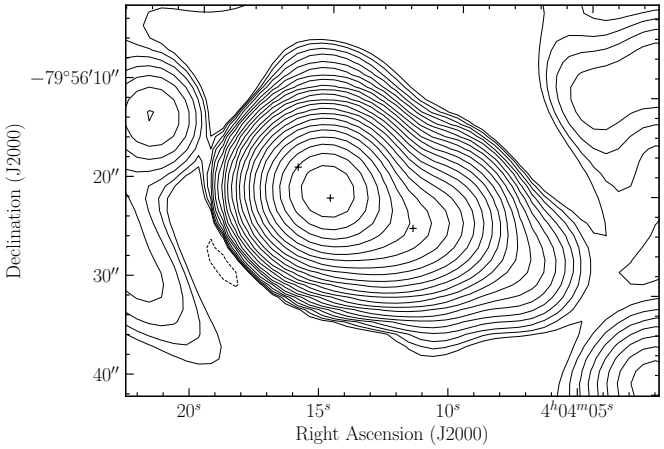

G05: 04:04:14.843 −79:56:21.4

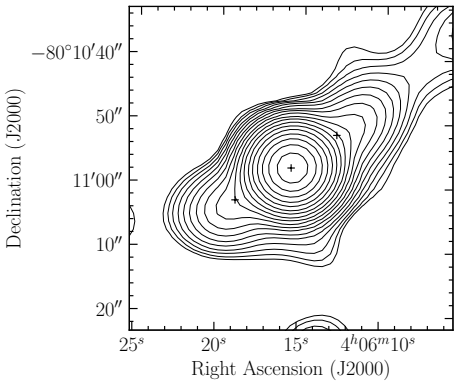

G06: 04:06:15.60 −80:10:57.4

Figure 13. Contour levels $\pm 5\,\mu$Jy beam$^{-1} \times 2^0, 2^{1/2}, 2^1, \ldots$ are plotted. Crosses mark the source group components.

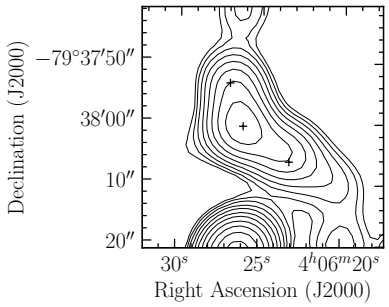

G07: 04:06:26.05 −79:38:00.9

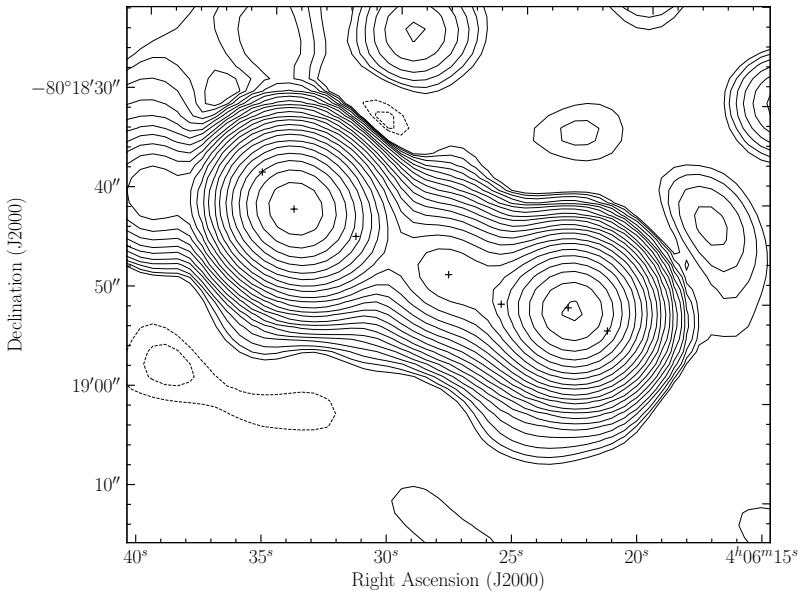

G08: 04:06:27.83 −80:18:47.9

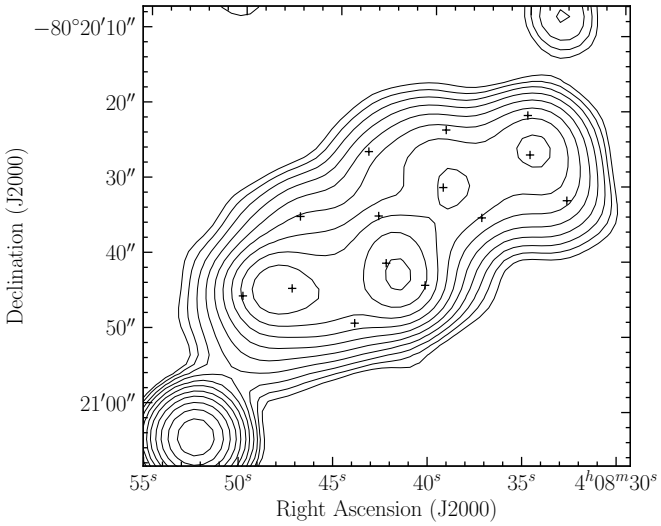

G09: 04:08:42.38 −80:20:40.8

Figure 14. Contour levels $\pm 5\,\mu\mathrm{Jy\,beam}^{-1} \times 2^0, 2^{1/2}, 2^1, \ldots$ are plotted. Crosses mark the source group components.

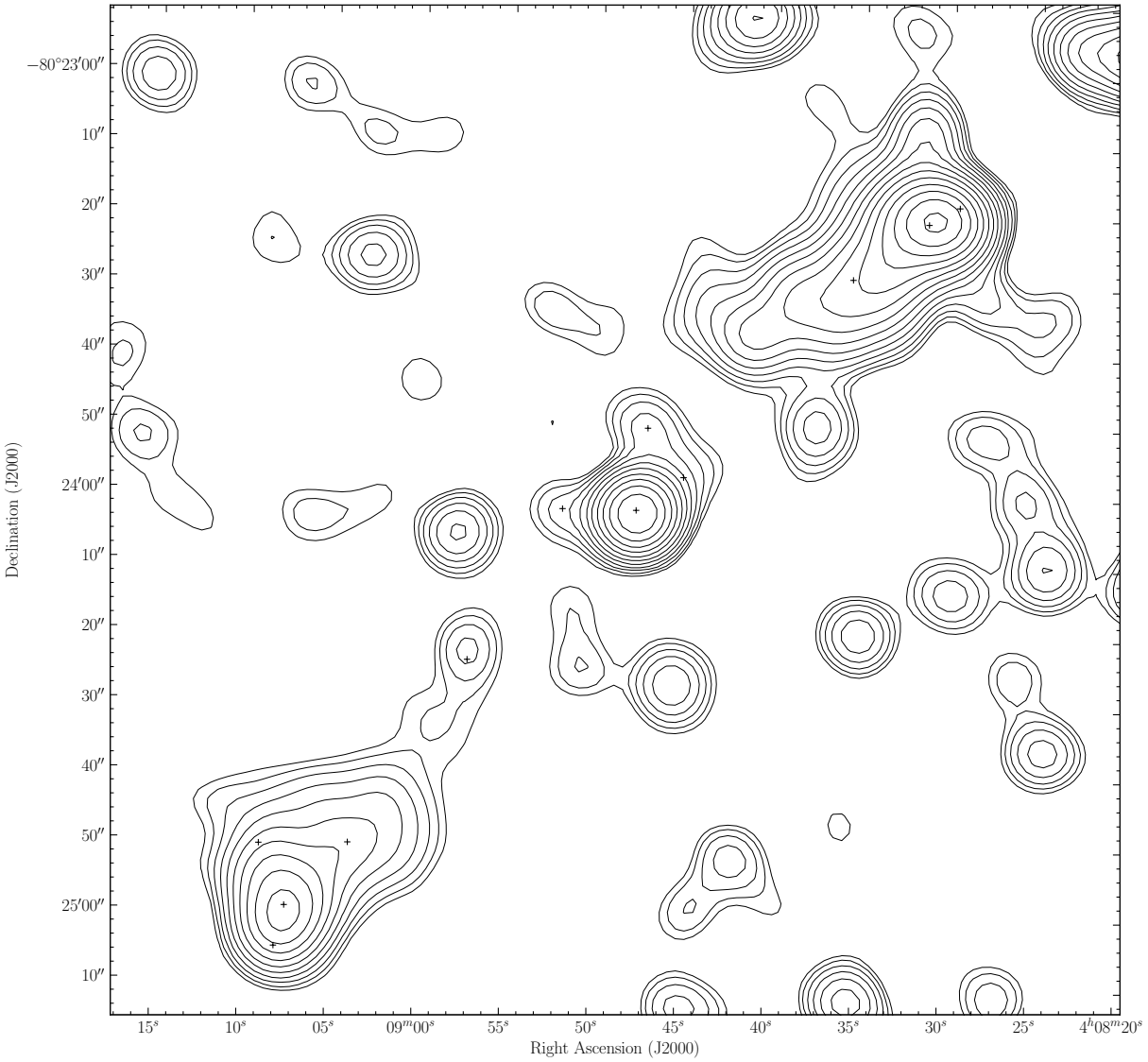

G10: 04:08:47.70 −80:24:02.3

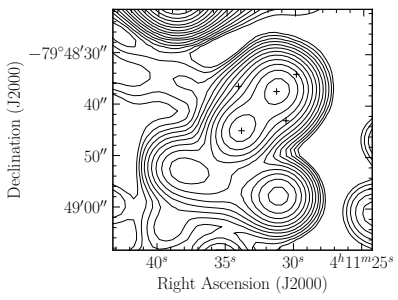

G11: 04:11:32.60 −79:48:41.2

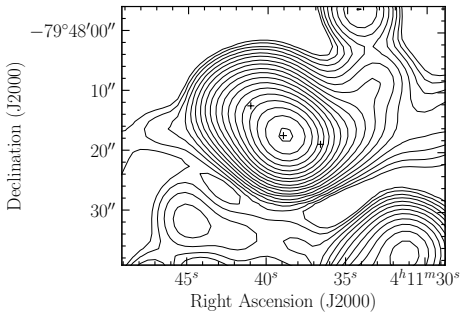

G12: 04:11:38.97 −79:48:17.4

Figure 15. Contour levels $\pm 5\,\mu\mathrm{Jy\,beam^{-1}} \times 2^0, 2^{1/2}, 2^1, \ldots$ are plotted. Crosses mark the source group components.

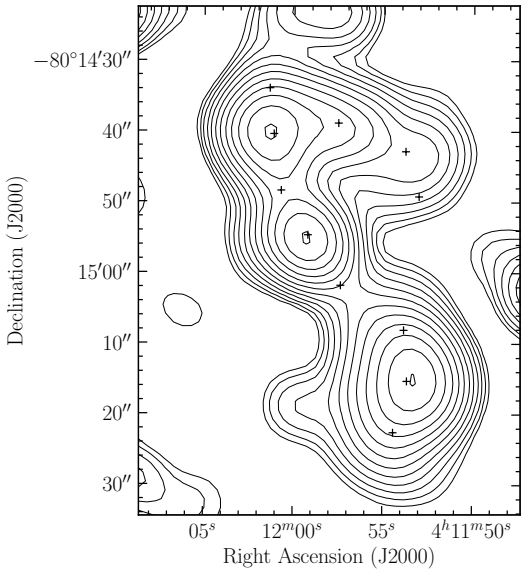

G13: 04:11:59.21 −80:14:54.7

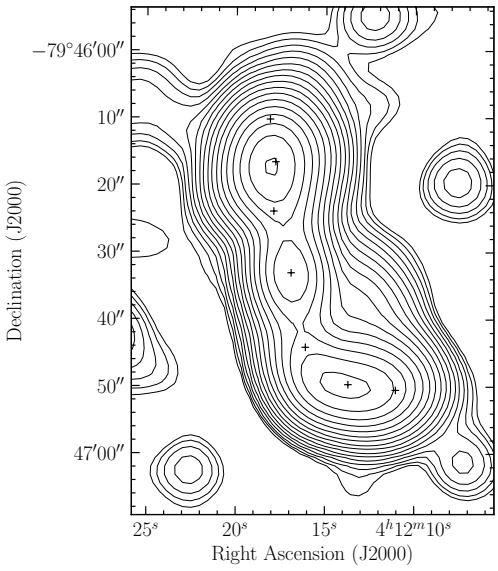

G14: 04:12:16.93 −79:46:33.1

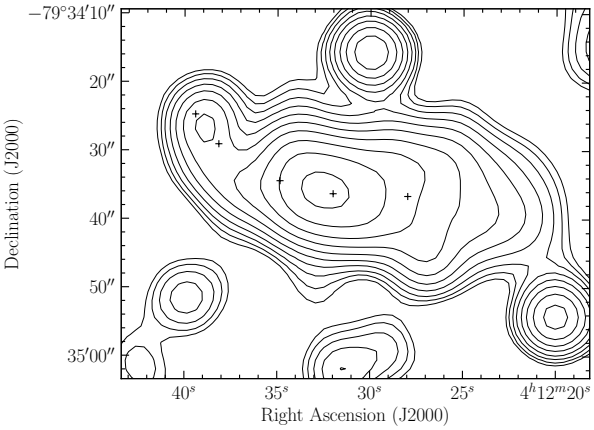

G15: 04:12:32.00 −79:34:36.3

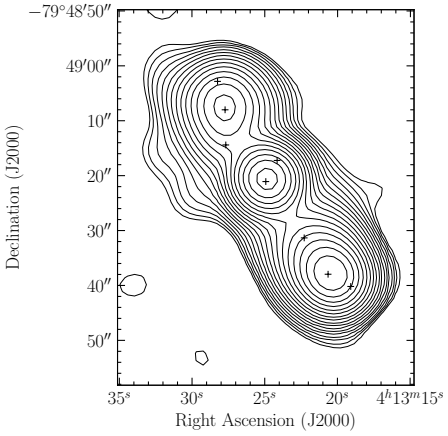

G16: 04:13:24.93 −79:49:21.1

Figure 16. Contour levels $\pm 5\,\mu\mathrm{Jy\,beam^{-1}} \times 2^0, 2^{1/2}, 2^1, \ldots$ are plotted. Crosses mark the source group components.

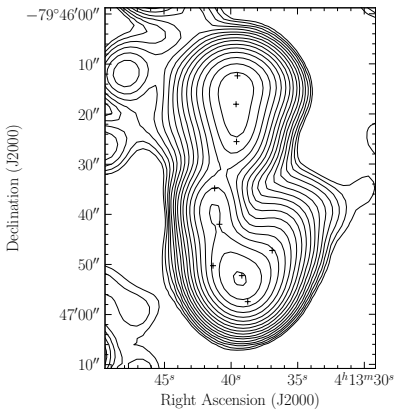

G17: 04:13:41.22 −79:46:34.8

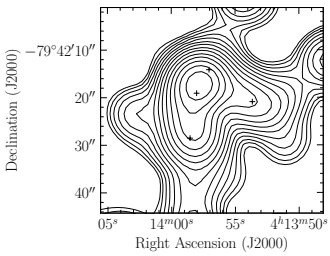

G18: 04:13:58.03 −79:42:19.1

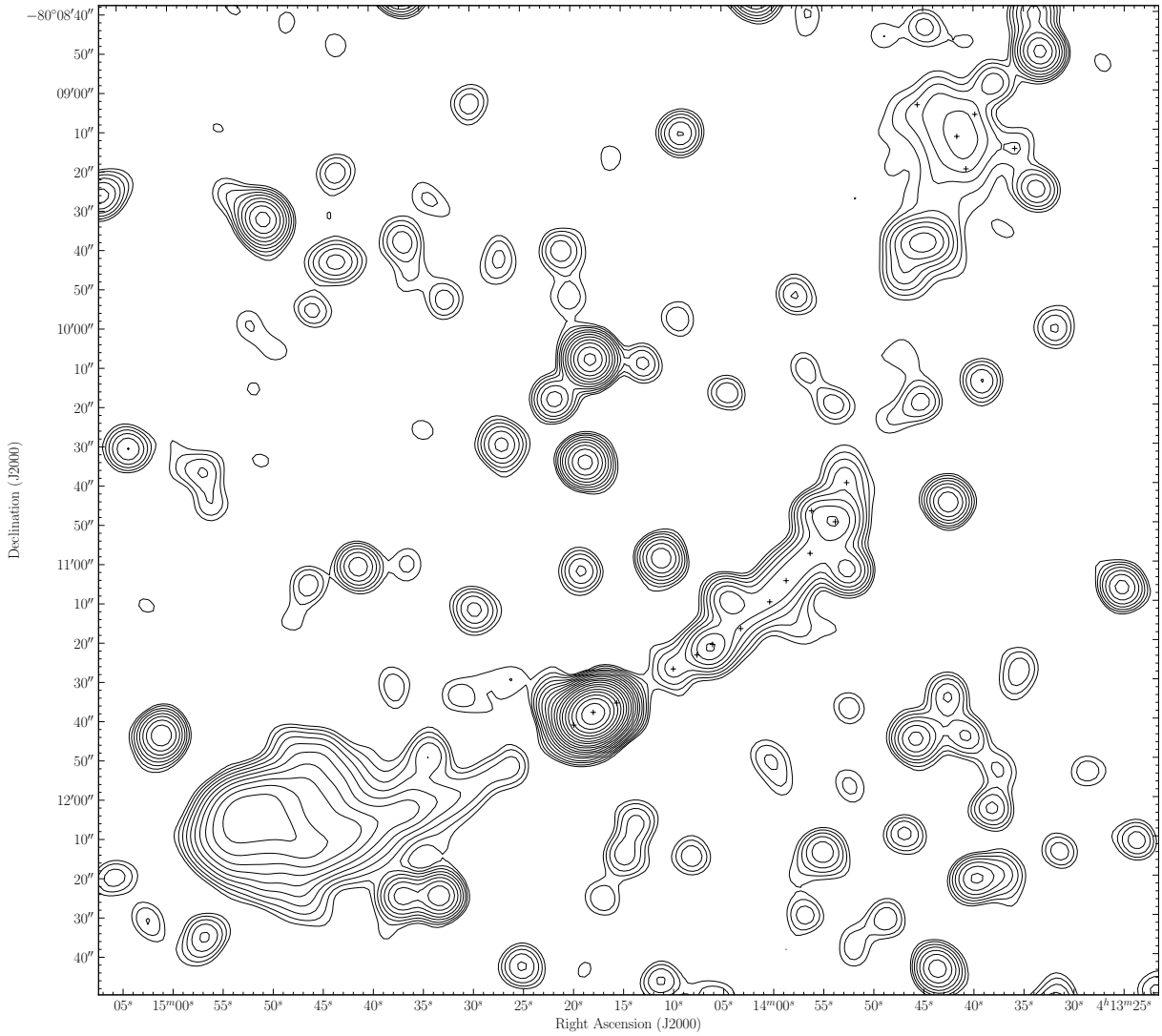

G19: 04:14:17.93 −80:11:38.3

Figure 17. Contour levels $\pm 5\,\mu\mathrm{Jy\,beam}^{-1} \times 2^0, 2^{1/2}, 2^1, \ldots$ are plotted. Crosses mark the source group components.

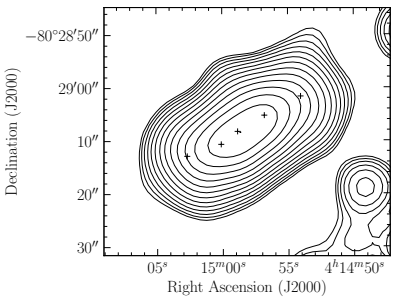

G20: 04:14:58.85 −80:29:08.3

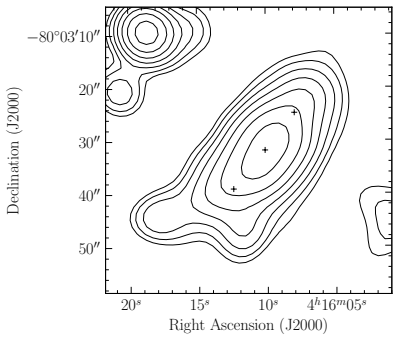

G21: 04:16:10.11 −80:03:31.8

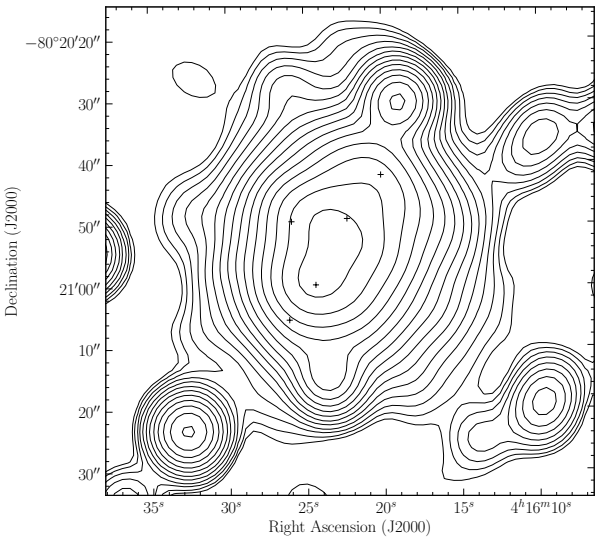

G22: 04:16:23.34 −80:20:54.4

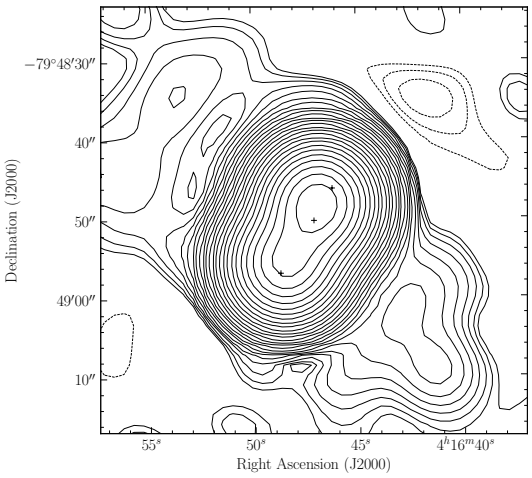

G23: 04:16:47.09 −79:48:50.2

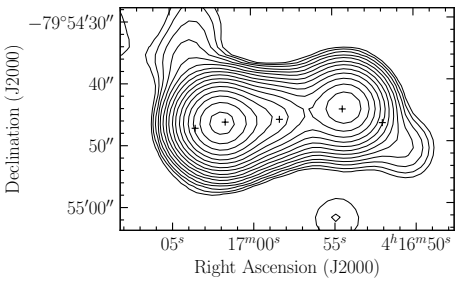

G24: 04:16:58.32 −79:54:46.1

Figure 18. Contour levels $\pm 5\,\mu\mathrm{Jy\,beam}^{-1} \times 2^0, 2^{1/2}, 2^1, \ldots$ are plotted. Crosses mark the source group components.

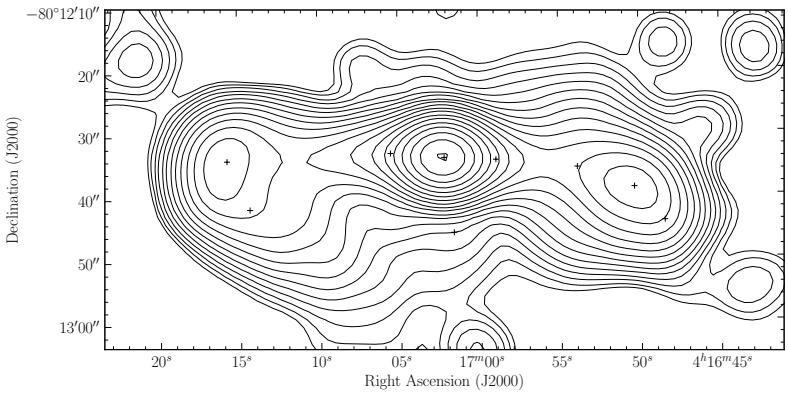

G25: 04:17:02.19 −80:12:33.8

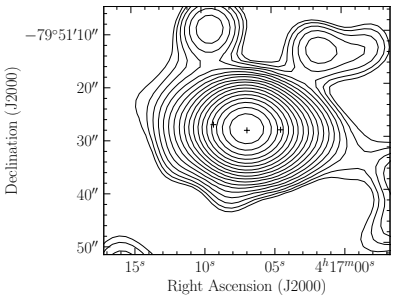

G26: 04:17:06.86 −79:51:28.5

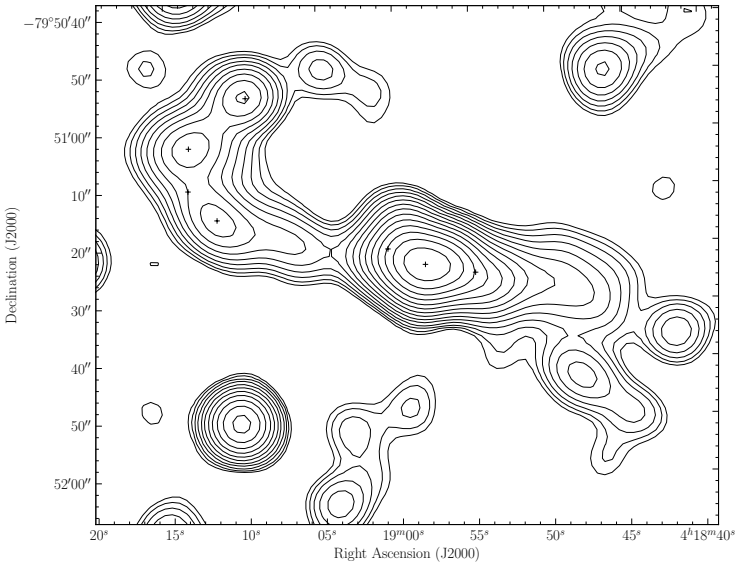

G27: 04:18:58.15 −79:51:23.4

Figure 19. Contour levels $\pm 5\,\mu\mathrm{Jy\,beam^{-1}} \times 2^0, 2^{1/2}, 2^1, \ldots$ are plotted. Crosses mark the source group components.

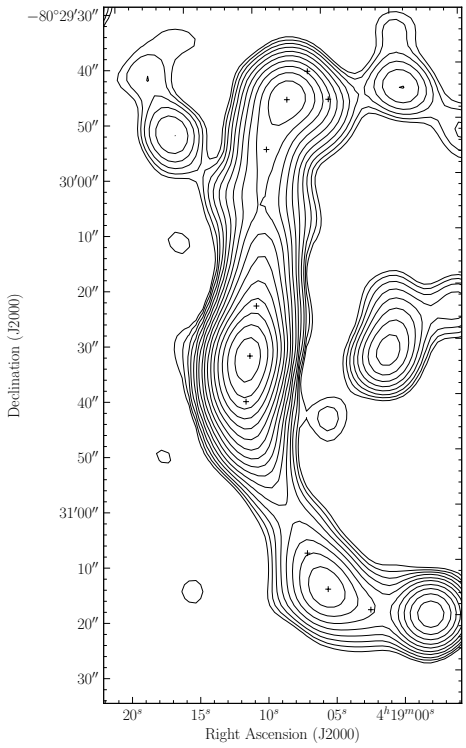

G28: 04:19:10.77 −80:30:32.3

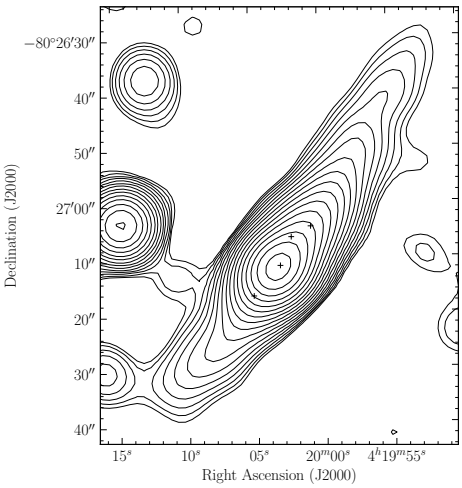

G29: 04:20:03.10 −80:27:11.2

Figure 20. Contour levels $\pm 5\,\mu\mathrm{Jy\,beam}^{-1} \times 2^0, 2^{1/2}, 2^1, \ldots$ are plotted. Crosses mark the source group components.

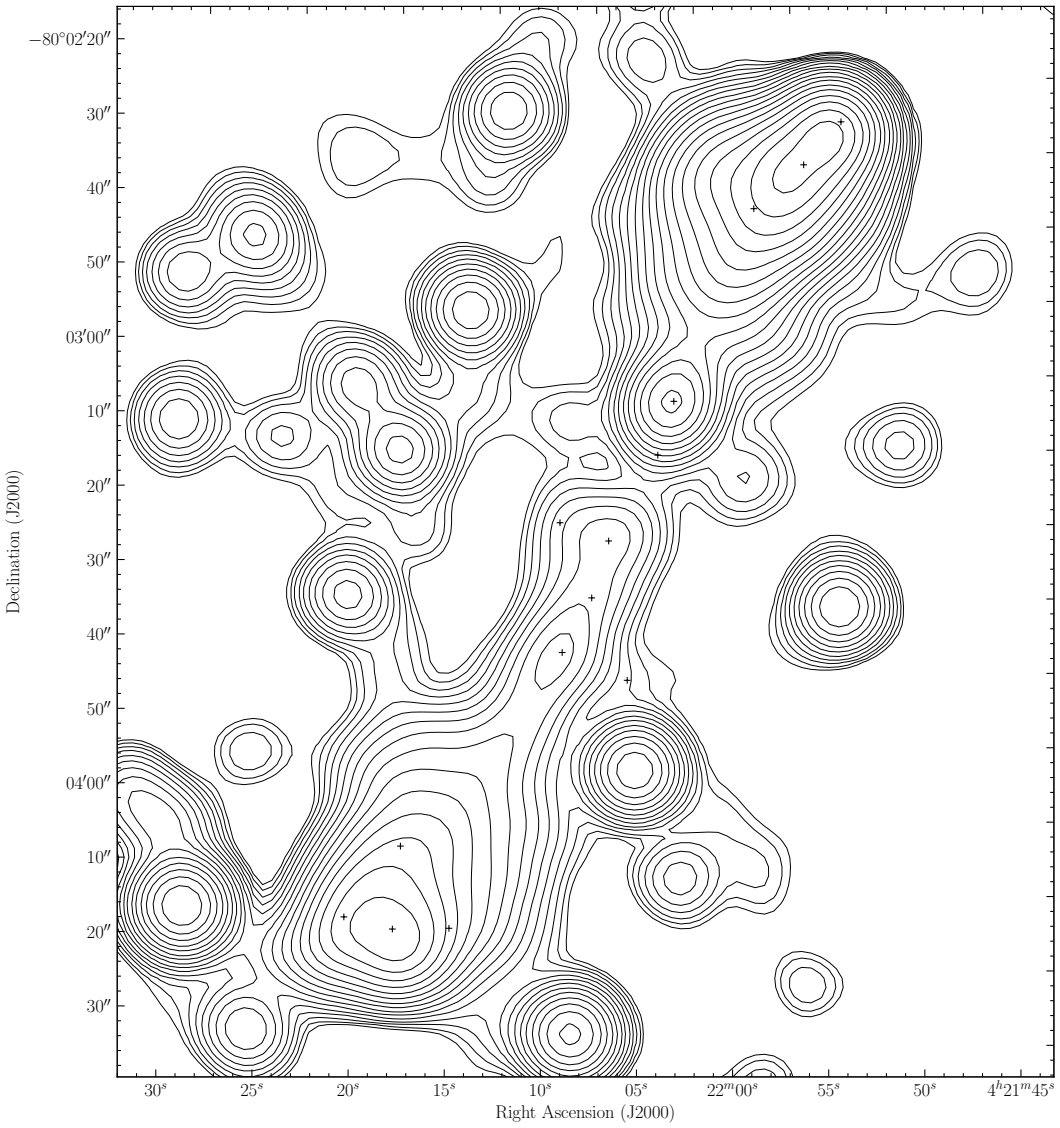

Figure 21. G30: 04:22:05.41 −80:03:30.0 Contour levels $\pm 5\,\mu\mathrm{Jy\,beam^{-1}} \times 2^0, 2^{1/2}, 2^1, \ldots$ are plotted. Crosses mark the source group components.

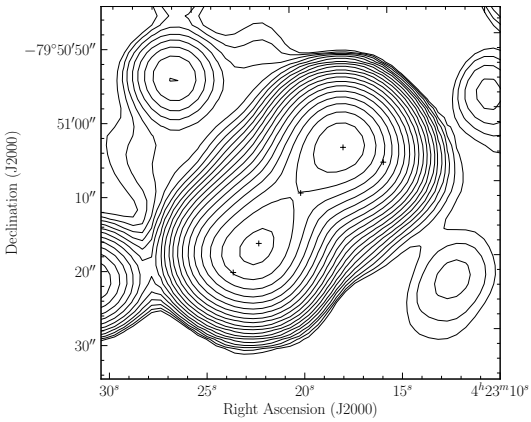

G31: 04:23:19.81 −79:51:10.5

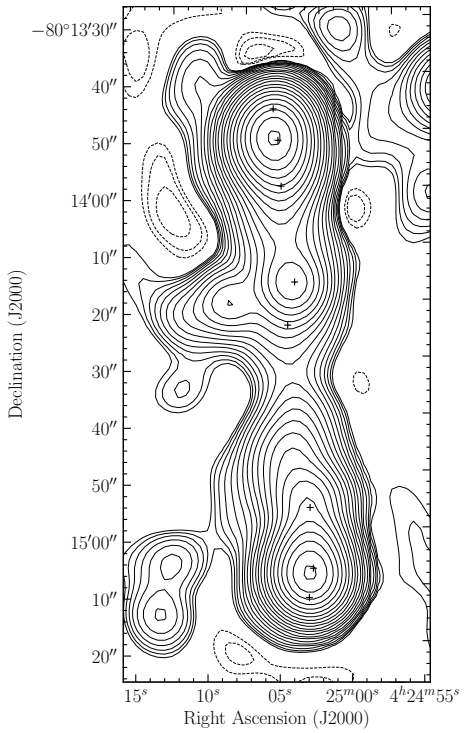

G32: 04:25:02.63 −80:14:15.8

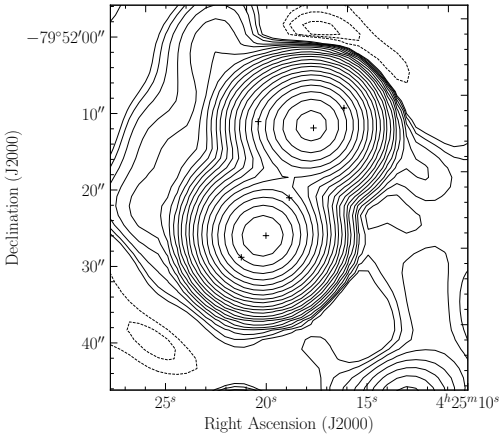

G33: 04:25:18.38 −79:52:22.2

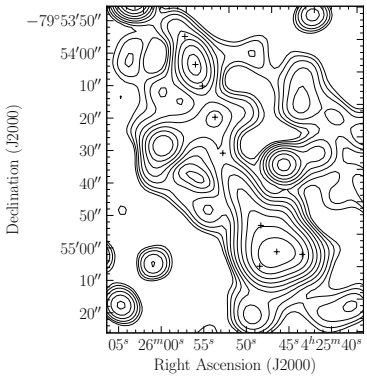

G34: 04:25:51.5 −79:54:38

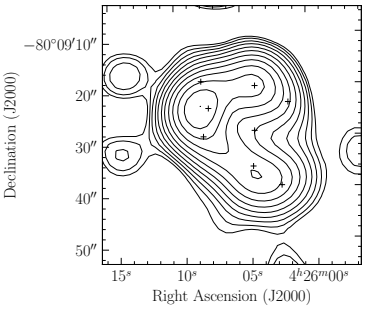

G35: 04:26:07.75 −80:09:23.6

Figure 22. Contour levels $\pm 5\,\mu\mathrm{Jy\,beam}^{-1} \times 2^0, 2^{1/2}, 2^1, \ldots$ are plotted. Crosses mark the source group components.